

Copyright Undertaking

This thesis is protected by copyright, with all rights reserved.

By reading and using the thesis, the reader understands and agrees to the following terms:

- 1. The reader will abide by the rules and legal ordinances governing copyright regarding the use of the thesis.
- 2. The reader will use the thesis for the purpose of research or private study only and not for distribution or further reproduction or any other purpose.
- 3. The reader agrees to indemnify and hold the University harmless from and against any loss, damage, cost, liability or expenses arising from copyright infringement or unauthorized usage.

IMPORTANT

If you have reasons to believe that any materials in this thesis are deemed not suitable to be distributed in this form, or a copyright owner having difficulty with the material being included in our database, please contact lbsys@polyu.edu.hk providing details. The Library will look into your claim and consider taking remedial action upon receipt of the written requests.

ADAPTIVE MODEL PREDICTIVE CONTROL OF UNMANNED UNDERWATER VEHICLES

YANG HU

MPhil

The Hong Kong Polytechnic University

2025

The Hong Kong Polytechnic University

Department of Aeronautical and Aviation Engineering

Adaptive Model Predictive Control of Unmanned Underwater Vehicles

Yang Hu

A thesis submitted in partial fulfilment of the requirements of the degree of Master of Philosophy

August 2024

CERTIFICATE OF ORIGINALITY

I hereby declare that this thesis is my own work and that, to the best of my knowledge and belief, it reproduces no material previously published or written, nor material that has been accepted for the award of any other degree or diploma, except where due acknowledgement has been made in the text.

Yang Hu

Abstract

Unmanned underwater vehicles (UUVs) are increasingly essential for a variety of underwater tasks, with a primary emphasis on achieving autonomy. Autonomy is critical for enhancing safety, flexibility, expanding operational capabilities, and reducing expenses. However, developing effective and robust control algorithms for UUVs is challenging due to nonlinear dynamics, uncertainties, constraints, and environmental disturbances. Model Predictive Control (MPC) is a well-established technique for UUV control, with the key challenge lying in obtaining precise prediction models to enhance controller performance.

This thesis primarily introduces two enhanced MPC approaches that enable a UUV with partially unknown dynamics to autonomously navigate complex marine environments. The first approach is a Disturbance Observer-based MPC (DOBMPC). The DOBMPC integrates unmodeled dynamics and environmental disturbances into a disturbance term estimated by an Extended Active Observer (EAOB). While the proposed DOBMPC effectively enhances disturbance rejection, the thesis also addresses handling unknown dynamics more meticulously.

Subsequently, the second proposed control method is an Adaptive MPC with an online system identification algorithm. This online system identification method is constructed using an Extended Active Observer (EAOB) and the Recursive Least Squares with Variable Forgetting Factor (RLS-VFF) algorithm to estimate environmental disturbances and identify uncertain hydrodynamic parameters. The estimated disturbances and parameters are continuously updated in the MPC's prediction model to generate optimal control

inputs based on real-time environmental and vehicle conditions.

These proposed methodologies are validated within the Gazebo and Robot Operating System (ROS) simulation environment, illustrating their effectiveness in managing uncertainties and disturbances for UUV control.

Keywords: model predictive control; disturbance observer; extended Kalman filter; adaptive control; unmanned underwater vehicle; online system identification;

Publications

- Y. Hu, B. Li, B. Jiang, J. Han, and C.-Y. Wen, "Disturbance observer-based model predictive control for an unmanned underwater vehicle," *Journal of Marine Science* and Engineering, vol. 12, no. 1, 2024.
- Y. Hu, B. Li, and C.-Y. Wen, "Adaptive model predictive control with online system identification for an unmanned underwater vehicle," in 2024 Oceans - Singapore, 2024.
- 3. L.-Y. Lo, Y. Hu, B. Li, C.-Y. Wen, and Y. Yang, "An adaptive model predictive control for unmanned underwater vehicles subject to external disturbances and measurement noise," in 2024 15th Asian Control Conference (ASCC), 2024.

Acknowledgements

I would like to express my sincere gratitude to my supervisor, Prof. Chih-Yung Wen, for his invaluable guidance, unwavering support, and insightful feedback throughout the course of my MPhil thesis. His expertise and encouragement have been instrumental in shaping this research.

I am also deeply thankful to my co-supervisor, Dr. Boyang Li, for his mentorship, encouragement, and scholarly input that have enriched this study.

Special thanks to Dr. Bing Wang for his valuable assistance, constructive criticism, and thoughtful suggestions that have significantly contributed to the development of this thesis.

I am also indebted to all my colleagues in the research group for their camaraderie, insightful discussions, and collaborative spirit. Your contributions and shared experiences have enriched this research journey in numerous ways.

Furthermore, I would like to extend my heartfelt appreciation to my family for their unconditional love, understanding, and constant encouragement. Their support has been a pillar of strength for me throughout this academic journey.

Thank you to all those who have contributed in ways seen and unseen to the completion of this thesis. Your support and encouragement have been invaluable.

Contents

Certificate of Originality

\mathbf{A}	bstra	ct	J
Pι	ıblic	ations	III
A	cknov	wledgements	V
C	onter	nts V	III
Li	${f st}$ of	Figures	ΧI
Li	${ m st}$ of	Tables	III
Li	st of	Abbreviations	ΚV
1	Intr	roduction	1
	1.1	Background	1
	1.2	Contributions	5
	1.3	Thesis Organization	6
2	Unr	nanned Underwater Vehicle Model	9
	2.1	Hardware and Software Design	9
	2.2	UUV Modeling	11

VII

5	Con	clusio	ns and Future Work	81
	4.4	Conclu	ısion	80
	4.3	Result	S	76
		4.2.4	Stability Analysis	74
		4.2.3	MPC Implementation	72
		4.2.2	Identification Algorithm	70
		4.2.1	Problem Formulation	69
	4.2	Metho	odology	68
	4.1	Litera	ture Review	65
4	Mo	del Pre	edictive Control with Online System Identification	65
	3.4	Concli	asion	61
	0.4	3.3.3	Results Analysis	
		3.3.2	Trajectory Tracking Results	
		3.3.1	Dynamic Positioning Results	
	3.3		S	
	0.0	3.2.3	MPC Implementation	
		3.2.2	Stability Analysis	
		3.2.1	Observer Design	
	3.2		odology	
	3.1		ture Review	
3			ce Observer-Based Model Predictive Control	27
		2.2.3	UUV Model for Motion Control	25
		2.2.2	Kinetic Model	16
		2.2.1	Kinematic Model	12

List of Figures

2.1	The software structure of the BlueROV2, incorporating a range of sensors	
	such as a stereo camera, DVL, AHRS, sonar, as well as an IMU and pressure	
	sensor connected to the Pixhawk	10
2.2	Front and rear perspectives of the fully assembled UUV	11
2.3	The reference frames of the UUV, including BRF and IRF	13
2.4	The propeller configuration of the BlueROV2, including two vertical pro-	
	pellers and four horizontal propellers	23
2.5	Thrust polynomial fitting based on PWM input value within 10-20 V	25
2.6	Thrust polynomial fitting results through fourth order fitting	26
3.1	Control loop of the MPC, which mainly includes an optimizer and a pre-	
	diction model	40
3.2	Block diagram of the proposed DOBMPC scheme with disturbance com-	
	pensation incorporated	44
3.3	Disturbances estimation of periodic waves with random force and moment	
	amplitudes	48
3.4	Tracking errors of the proposed DOBMPC, baseline MPC and PID con-	
	trollers under periodic disturbances	49
3.5	Trajectories of dynamic positioning results of the proposed DOBMPC,	
	baseline MPC and PID controllers under periodic disturbances	49

3.6	Control inputs of the proposed DOBMPC in surge, sway, heave and yaw	
	direction for dynamic positioning under periodic wave effect	50
3.7	Disturbances estimation of constant currents in x, y, z directions	51
3.8	Tracking errors of the proposed DOBMPC, baseline MPC, and PID con-	
	trollers under constant currents	52
3.9	Trajectories of dynamic positioning results of the proposed DOBMPC,	
	baseline MPC, and PID controllers under constant currents	53
3.16	Circular trajectory tracking results of the proposed DOBMPC, baseline	
	MPC, and PID controllers in x, y, z, and yaw directions	53
3.10	Control inputs of the proposed DOBMPC in surge, sway, heave and yaw	
	direction for dynamic positioning under constant currents	54
3.17	Three-dimensional circular trajectory tracking results of the proposed DOBMP	'С,
	baseline MPC, and PID controllers	54
3.11	Disturbances estimation of superposition of periodic wave and constant	
	current effect in x, y, z directions	55
3.18	Control inputs of the proposed DOBMPC in surge, sway, heave, and yaw	
	direction for tracking circular trajectory under constant currents	55
3.12	Tracking errors of the proposed DOBMPC, baseline MPC, and PID con-	
	trollers under superposition of periodic wave and constant current effect	56
3.13	Control inputs of the proposed DOBMPC in surge, sway, heave and yaw	
	direction for dynamic positioning under superposition of periodic wave and	
	constant current effect	57
3.20	Lemniscate trajectory tracking results of the proposed DOBMPC, baseline	
	MPC, and PID controllers in x, y, z, and yaw directions	57
3.14	Disturbances estimation of constant currents during circular trajectory	
	tracking	58

3.21	Tracking errors of the proposed DOBMPC, baseline MPC, and PID con-	
	trollers under constant currents during lemniscate trajectory tracking	58
3.15	Tracking errors of the proposed DOBMPC, baseline MPC, and PID con-	
	trollers under constant currents during circular trajectory tracking	59
3.22	Three-dimensional lemniscate trajectory tracking results of the proposed	
	DOBMPC, baseline MPC, and PID controllers	59
3.19	Disturbances estimation of periodic waves during lemniscate trajectory	
	tracking	60
3.23	Control inputs of the proposed DOBMPC in surge, sway, heave, and yaw	
	direction for tracking lemniscate trajectory under periodic waves	60
4.1	Block diagram of the proposed adaptive MPC scheme for the UUV, where	
	the blue box illustrates baseline MPC and control allocation, the yellow	
	box shows the UUV platform, and the pink module indicates the adaptive	
	module with an observer and identification algorithm	74
4.2	Online system identification results of added mass, linear damping coef-	
	ficients, nonlinear damping coefficients, and environmental disturbances	
	using the Recursive Least Squares with Forgetting Factor (RLS-FF) and	
	the Recursive Least Squares with Variable Forgetting Factor (RLS-VFF)	
	during the training process without applied environmental disturbances	77
4.3	Online system identification results of added mass, linear damping coeffi-	
	cients, nonlinear damping coefficients, and environmental disturbances us-	
	ing the RLS-FF and the RLS-VFF during the training process with applied	
	environmental disturbances	78
4.4	Control results of lemniscate trajectory tracking using the proposed adap-	
	tive MPC, standard MPC, and PID controllers	79

List of Tables

2.1	Notations in the UUV dynamic model	12
3.1	BlueROV2 rigid-body parameters defined in URDF file	46
3.2	BlueROV2 hydrodynamic parameters defined in URDF file	46
3.3	MPC parameters utilized in this work	47
3.4	PID parameters utilized in this work	47
3.5	RMSE of the proposed DOBMPC, baseline MPC, and PID controllers in	
	dynamic positioning and trajectory tracking	62

List of Abbreviations

UUV Unmanned Underwater Vehicle

ROV Remotely Operated Vehicle

AUV Autonomous Underwater Vehicle

DOF Degrees of Freedom

MIMO Multiple-Input Multiple-Output

PID Proportional-Integral-Derivative

MPC Model Predictive Control

EKF Extended Kalman Filter

ROS Robot Operating System

NMPC Nonlinear Model Predictive Control

SMC Sliding Mode Control

NN Neural Network

QP Quadratic Programming

NLP Nonlinear Programming

OCP Optimal Control Problem

DO Disturbance Observer

DOBC Disturbance Observer-Based Control

NDO Nonlinear Disturbance Observer

ADRC Active Disturbance Rejection Control

ESO Extended State Observer

DOBMPC Disturbance Observer-Based Model Predictive Control

AMPC Adaptive Model Predictive Control

BRF Body-Fixed Reference Frame

IRF Inertial Reference Frame

CG Center of Gravity

CB centre of buoyancy

ECI Earth-Centered Inertial

ECEF Earth-Centered Earth-Fixed

NED North-East-Down

PWM Pulse Width Modulation

SQP Sequential Quadratic Program

URDF Unified Robot Description Format

RMSE Root Mean Square Error

DVL Doppler Velocity Log

AHRS Attitude and Heading Reference System

XVI

EAOB Extended Active Observer

LS Least Square

RLS Recursive Least Square

VFF Variable Forgetting Factor

RLS-FF Recursive Least Squares with Forgetting Factor

RLS-VFF Recursive Least Squares with Variable Forgetting Factor

PWNN Piecewise White Noise Model

RK4 Fourth-Order Runge-Kutta

USBL Ultra-Short Baseline

GPS Global Positioning System

AHRS Attitude and heading reference system

DVL Doppler Velocity Log

MAE Mean Absolute Error

GP Gaussian Process

IMU Inertial Measurement Unit

TMPC Tube Model Predictive Control

CD-EKF Continuous-Discrete Extended Kalman Filter

Chapter 1

Introduction

This chapter provides a brief introduction of the research work, which includes the background information about the Unmanned Underwater Vehicle (UUV), the motivation of the research work, and the current contributions. The organization of the thesis is presented at the end of this chapter.

1.1 Background

With the increasing demand for underwater operations, UUVs have gained significant interest for applications in a variety of challenging underwater tasks, such as underwater facilities repair operations [1], marine-growth removal [2], and offshore infrastructure inspection [3]. These applications serve as representative examples of proving the effectiveness of using UUVs in assisting or even replacing humans in hazardous and labor-intensive tasks. UUVs represent an integration of various disciplines, combining mechanical, sensor fusion, electrical design, communication systems, and control systems. Through their integrated technology and remarkable accomplishments, UUVs became invaluable tools for improving underwater operations' efficiency and safety.

Coastal cities such as Hong Kong heavily rely on large-scale bridges as essential trans-

portation infrastructure. Yet, severe weather, such as typhoons, strong winds, and seawater corrosion, can accelerate degradation and pose serious problems for these structures. Consequently, routine bridge inspections prove crucial for identifying issues early on and recommending the necessary maintenance to guarantee sustainability and safety of these structures. Traditionally, human divers are employed for underwater bridge inspection tasks. Nevertheless, the unpredictable and complex underwater conditions around offshore structures increase the dangers associated with human-led inspections. The range of access available to human divers is also constrained. In contrast, UUVs offer numerous benefits in inspection tasks in underwater environments, including reducing operation cost, improving efficiency, and enhancing safety. UUVs can feedback high-resolution data in real time, navigate in complex areas, and conduct thorough inspections without human intervention, making them ideal for maintaining the safety and reliability of coastal bridges.

UUVs can be categorized into two kinds, which are Remotely Operated Vehicle (ROV) and Autonomous Underwater Vehicle (AUV). This classification is based on the extent of human involvement during their mission execution processes. ROVs often heavily rely on human instructions during operations. Therefore, a tether is required for signal and data transmitting between vehicles and human operators in real time. In contrast, AUVs have a higher level of autonomy, which allows them to execute pre-programmed missions off-line. This autonomy allows AUVs to travel longer distances and minimize human operation costs. As a result, the current focus of UUV development is concentrated on increasing autonomy, while the autonomy highly depends on the design of control systems.

Designing control systems for UUVs presents several significant challenges. Firstly, UUVs are Multiple-Input Multiple-Output (MIMO) dynamic systems that are highly nonlinear. Besides, parametric uncertainties pose a consideration problem. These uncertainties are caused by the difficulty of accurately identifying hydrodynamic coefficients. which capture the complex interactions between the UUV and the surrounding fluid.

Estimating the dynamic loading on the vehicle caused by hydrodynamic terms associated with waves and currents further complicates the matter, especially during aggressive maneuvering. Another major challenge involves coping with unpredictable time-varying environmental disturbances in complex underwater environments, such as ocean waves and currents. Operating under such conditions can lead to instability and performance degradation in the closed-loop control system, hindering even simple inspection tasks. Therefore, it is crucial to effectively address these problems in UUV control systems.

Numerous control approaches have been developed to tackle the aforementioned control challenges. Traditionally, the Proportional-Integral-Derivative (PID) control method has been used to address motion control problems in autonomous vehicles. PID control offers a cost-effective and easily implementable solution. It is beneficial due to its model-free nature and ability to provide system stability by adjusting the control signal based on the error between the desired setpoint and the actual process variable. In order to enhance robustness against external disturbances, an adaptive fuzzy nonlinear PID controller was developed for an underwater robotic vehicle [4].

Another popular control method is Sliding Mode Control (SMC). Unlike the model-free PID approach, SMC addresses the issue of parametric uncertainty by creating a sliding surface that the system's state trajectory is compelled to follow, regardless of uncertain parameters. In order to achieve closed-loop stability, a robust adaptive SMC was designed for an underactuated AUV [5]. The stability of this proposed method was also proved by using Lyapunov's direct method. However, SMC suffers from chattering problems, which is a phenomenon arising due to SMC's discontinuous control law. This chattering effect can result in reduced accuracy and energy loss, especially when the vehicle operates at high speeds.

In recent years, Model Predictive Control (MPC) methods have exploded in popularity, driven by advances in on-board computer computing capabilities [6]. MPC involves solving an Optimal Control Problem (OCP) with a finite horizon recursively to determine

the control action at every time step. MPC is particularly favored for designing control systems for UUVs due to its ability to handle control limits and state constraints. Furthermore, Nonlinear Model Predictive Control (NMPC) provides additional advantages by accommodating the inherent nonlinear dynamics of complex systems. However, it is important to note that the performance of MPC is heavily dependent on the accuracy of the prediction model used.

Consequently, several improved MPC methods have been developed to enhance the performance of the controller. One common approach is employing a Disturbance Observer (DO) that estimates and compensates for unmodeled dynamics and disturbances, in order to overcome the parametric uncertainties and environmental disturbances. The combination of MPC and DOB has been proposed and implemented in many recent research studies. For example, a robust MPC based on Active Disturbance Rejection Control (ADRC) was developed for an AUV [7]. This approach implemented a discrete Extended State Observer (ESO) to estimate the effect of model uncertainties and external disturbances. Data-driven methods have also been widely applied to learn dynamic residuals, which enhance the prediction model incorporated in MPC. A MPC framework with learned residual dynamics using Gaussian Processes was proposed in 2021 [8]. It aimed to improve control performance in high-speed trajectory tracking problems by providing a more accurate dynamics model. While these research works have demonstrated enhanced robustness and control performance by addressing external disturbances and model uncertainties, they still have certain limitations. Disturbance Observer-Based Control (DOBC) methods treat unmodeled dynamics as part of disturbances to be compensated, which does not provide an accurate model for MPC. As for data-driven methods, they typically require a large amount of training data, which can lead to heavy computational burden.

Based on existing challenges in control and their solutions, this research project aims to offer a reliable control resolution for enabling UUVs to conduct autonomous inspections of bridges. The main focus of this study lies within the domain of control systems, where

two types of Adaptive Model Predictive Control (AMPC) are introduced. The initial approach develops a Disturbance Observer-Based Model Predictive Control (DOBMPC), which using an Extended Active Observer (EAOB) to estimate total disturbances, including unmodeled dynamics and environmental disturbances. Subsequently, to address disturbances more effectively, instead of combining all sources of disturbance into a single variable per Degrees of Freedom (DOF) through the principle of superposition, the second method aims to establish an AMPC integrated with an online system identification module. This module is designed to identify uncertain hydrodynamic parameters using the overall estimated disturbances provided by the EAOB. To realize this, the RLS-VFF algorithm is employed to iteratively update the estimated parameters within the MPC's prediction model. The RLS-VFF algorithm not only adjusts to non-static data and dynamically changing system behaviors but also enhances memory efficiency, making the method both practical and cost-efficient. The dynamic adaptation of the variable forgetting factor within the algorithm is guided by the F-test, strengthening its capability to detect and react to the changes in the system. To achieve autonomous navigation, the UUV adopted in this study is also equipped with multiple sensors, including a sonar, a Doppler Velocity Log (DVL), a pressure sensor, an Attitude and heading reference system (AHRS), and a stereo camera. Although the autonomous navigation module is still under development due to time limitations, the hardware and software design part has been finalized and is described within this study.

1.2 Contributions

The primary objective of this project is to effectively tackle the challenges arising from complex varying marine environments and evolving system dynamics, ultimately delivering a robust solution that enables UUVs to autonomously operate in complex underwater environments. The main contributions of this research are outlined as follows:

- 1. Development of a baseline NMPC approach that considers physical system constraints, including control inputs and system state limitations. The prediction model within the NMPC will be continuously updated using feedback from a disturbance observer and an online parameter estimation module. This update process will create a parameter-varying model.
- 2. Development of an EAOB to estimate total disturbances, encompassing both unmodeled dynamics and external disturbances. The estimated disturbances will be provided to the online parameter estimation algorithm. The objective is to achieve accurate estimations even in the presence of measurement noise.
- 3. Design of a learning-based online identification algorithm for real-time adaptation and learning of the dynamics of the UUV. By utilizing the disturbances provided by the EAOB, the learning problem is simplified, enabling the development of an accurate data-augmented dynamic model for the NMPC.

1.3 Thesis Organization

The following chapters of this thesis are organized as below:

- Chapter 2 presents a foundational description of the UUV model utilized, encompassing the hardware and software design, and dynamic modeling of the UUV.
- Chapter 3 introduces the initial control method proposed in this study, namely DOBMPC. This chapter entails a review of literature on various forms of DOBC, the methodology of the proposed approach, results from semi-physical experiments, and concluding insights.
- Chapter 4 demonstrates the development of the second control method, derived from Chapter 3, which is an AMPC integrated with online system identification. It

incorporates a review of related adaptive control methods utilizing data-augmented models, the methodology of the identification algorithm and MPC implementation, results from identification and control performance, and conclusions.

• Chapter 5 summarizes the work in this thesis and discusses the future works and research directions.

Chapter 2

Unmanned Underwater Vehicle Model

This chapter primarily focuses on introducing the model of the selected UUV platform, encompassing its hardware and software design as well as dynamic modeling. The hardware and software design section elaborates on the sensors integrated into the UUV platform and their intercommunication. In the dynamic modeling segment, a comprehensive dynamic model is developed, serving as a foundation for constructing model-based controllers in subsequent chapters.

2.1 Hardware and Software Design

The research employs the BlueROV2 as the foundational UUV platform. While the full navigation module remains unfinished, the project has successfully implemented sensor installation and communication, laying a groundwork for future navigation algorithm development. The BlueROV2 features a Pixhawk as a flight controller, a Raspberry Pi as a companion computer, and a USB camera connected to the companion computer. The Pixhawk includes an onboard Inertial Measurement Unit (IMU) and pressure sensor, with data transmitted to MAVProxy and MAVROS via USB. MAVProxy relays messages via UDP to QGroundControl on the topside computer, which also receives USB camera data

through gstreamer. MAVROS operates within the companion computer's ROS environment. The stereo camera and AHRS communicate with the companion computer through serial connections, enabling the companion computer's Robot Operating System (ROS) to run drivers for these sensors, facilitating sensor data integration within ROS. Sonar and DVL connect to the companion computer via an Ethernet switch, allowing SonarView on the topside computer to receive sonar data. A DVL ROS driver on the topside computer processes DVL data, publishing it as ROS topics. With ROS nodes running on both the companion and topside computers, they engage in multiple ROS communications, configuring the companion computer as a ROS slave and the topside computer as a ROS master to consolidate sensor data within ROS. Figure 2.1 illustrates the overall software structure of the developed BlueROV2.

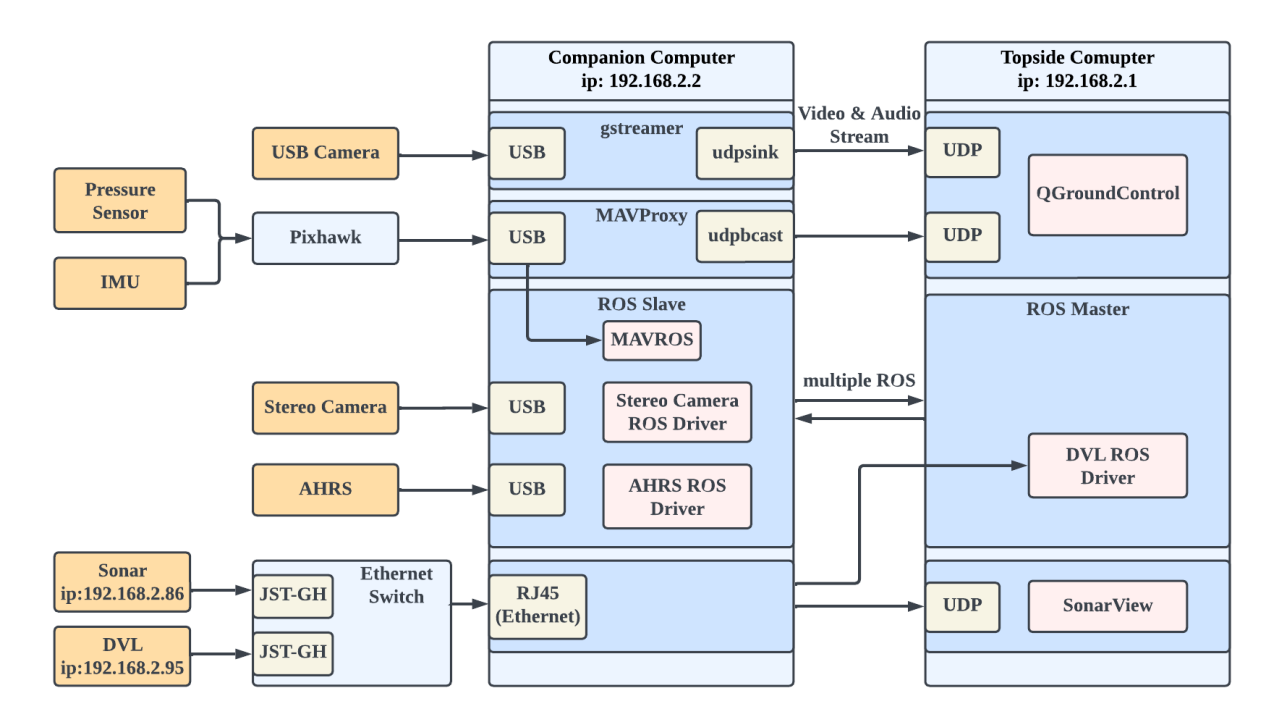


Figure 2.1: The software structure of the BlueROV2, incorporating a range of sensors such as a stereo camera, DVL, AHRS, sonar, as well as an IMU and pressure sensor connected to the Pixhawk.

Figure 2.2 illustrates the physical arrangement of sensors within the BlueROV2. The stereo camera and sonar are situated on an extended payload skid, enabling them to face





Figure 2.2: Front and rear perspectives of the fully assembled UUV.

forward to execute perception and mapping functions. Positioned at the rear, the DVL is shielded from disturbances caused by the fluid surrounding the thrusters, safeguarding the accuracy of its measurements. The AHRS is housed within a sealed tube, aligned with the orientation of the onboard IMU to facilitate calibration procedures.

2.2 UUV Modeling

The analysis of UUV motion model can be categorized into two main groups: kinematics, which focuses solely on the geometric aspects of motion, and kinetics, which examines the forces and moments that drive the motion. In this section, it provides detailed explanations of the kinematic and kinetic equations governing UUV motion. Based on these equations, a control system model can be established as a basis for the study of UUV motion control. The section has been included as a part of the author's published paper [9].

In this research work, we selected BlueROV2 [10] which has 4 degrees of freedom as the UUV platform, which operates with 4 DOF covering surge, sway, heave, and yaw movements. To characterize the UUV's motion, we employ Fossen's principles [11], encompassing rigid body dynamics, added mass effects, and damping. This section elaborates

rates on the detailed kinematic and kinetic equations that govern the motion of the UUV. These equations form the basis for constructing a system model for motion control. The parameters' symbols derived from the dynamic model of the UUV are outlined in Table 2.1.

	Surge Sway Heave	Roll Pitch Yaw
Position η	x y z (m)	$\phi \theta \psi (rad)$
Velocity $oldsymbol{v}$	$u \ v \ w \ (m/s)$	$p \ q \ r \ (rad/s)$
Forces and Moments $\boldsymbol{\tau}$	X Y Z (N)	K M N (Nm)
Control Inputs \boldsymbol{u}	$u_1 \ u_2 \ u_3 \ (N)$	$/ \ / \ u_4 \ (Nm)$
Total Disturbances \boldsymbol{w}	$X_w Y_w Z_w (N)$	$K_w M_w N_w (Nm)$
Environmental Disturbance $\boldsymbol{\tau}_{\text{env}}$	$X_{ m env} \ Y_{ m env} \ Z_{ m env}$	$K_{ m env}~M_{ m env}~N_{ m env}$
Unmodeled dynamics Δau	$\Delta X \ \Delta Y \ \Delta Z$	$\Delta K \ \Delta M \ \Delta N$
Added Mass $\boldsymbol{M_A}$	$X_{\dot{u}} Y_{\dot{v}} Z_{\dot{w}} (kg)$	$K_{\dot{p}} M_{\dot{q}} N_{\dot{r}} (kgm^2/rad)$
Linear Damping $\boldsymbol{D_L}$	$X_u Y_v Z_w (Ns/m)$	$K_p M_q N_r (Ns/rad)$
Nonlinear Damping $oldsymbol{D_{NL}}$	$X_{u u } Y_{v v } Z_{w w } (Ns^2/m^2)$	$K_{p p } M_{q q } N_{r r } (Ns^2/rad^2)$
Feedback Variables	x y z (m)	$\phi \; \theta \; \psi \; (rad)$
	$u \ v \ w \ (m/s)$	$p \ q \ r \ (rad/s)$
	X Y Z (N)	$/\ /\ N_w\ (Nm)$

2.2.1 Kinematic Model

Reference Frames

In general, two reference frames are typically employed to depict the motion states of the UUV, as illustrated in Figure 2.3, namely the Body-Fixed Reference Frame (BRF) and the Inertial Reference Frame (IRF).

• The BRF is affixed to the vehicle, with the Center of Gravity (CG) designated as the origin. The body axes align with the principal axes of inertia. The longitudinal axis, denoted as the x_b axis, extends from aft to fore. The transversal axis, known as the y_b axis, extends from port to starboard. Per the right-hand rule, the z_b axis is orthogonal to both the x_b and y_b axes.

• The UUV's motion can be delineated as the movement of the BRF concerning an IRF. The IRF is instrumental in monitoring the vehicle's path and specifying control objectives. Commonly used IRFs encompass the Earth-Centered Inertial (ECI)frame, the Earth-Centered Earth-Fixed (ECEF) reference frame, and the North-East-Down (NED) coordinate system. In this study, the IRF aligns with the NED coordinate system, a selection driven by the widespread adoption of NED coordinates for expressing position vectors in diverse navigation applications and simulation settings. The axes in the IRF are labeled as x_i , y_i , and z_i , as depicted in Figure 2.3.

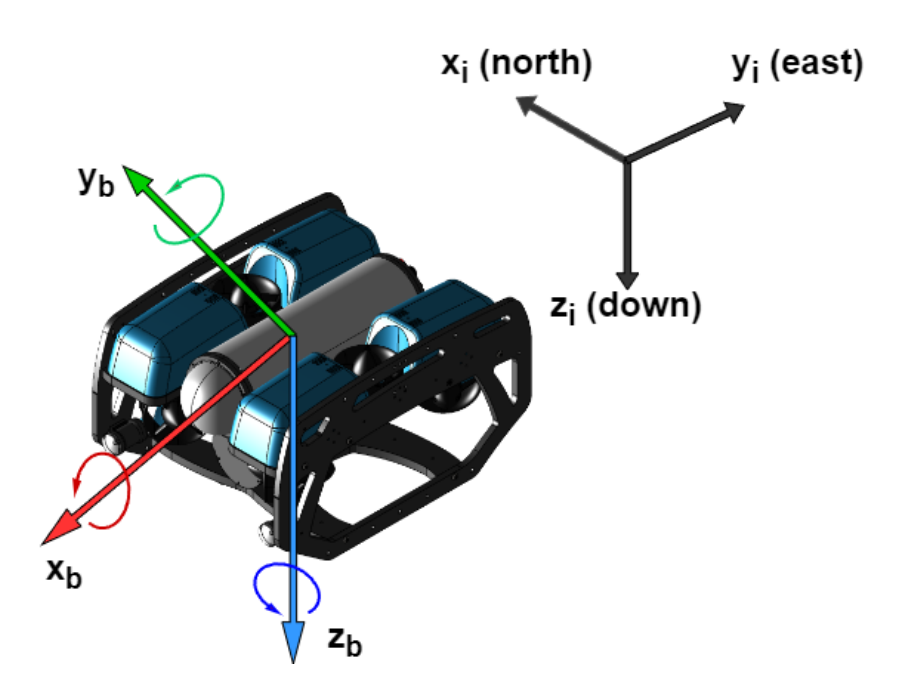


Figure 2.3: The reference frames of the UUV, including BRF and IRF.

In the UUV's model states, the linear and angular velocities are described in the BRF as $\eta = [x, y, z, \phi, \theta, \psi]^{T}$, while the linear and angular position are expressed in the IRF as $\mathbf{v} = [u, v, w, p, q, r]^{T}$.

In this study, the decision is made to align the IRF with the NED coordinate system.

This choice is influenced by the common practice of representing position vectors using NED coordinates across a wide range of navigation applications and simulation contexts.

Transformations Between Reference Frames

Since the velocity vector and position vector are expressed in different reference frames, the rotation matrix \mathbf{R}_b^i , which is an element in SO(3), are required for describing the relationship between them:

$$SO(3) = \left\{ \boldsymbol{R} \mid \boldsymbol{R} \in \mathbb{R}^{3 \times 3}, \boldsymbol{R} \boldsymbol{R}^{\mathrm{T}} = \boldsymbol{R}^{\mathrm{T}} \boldsymbol{R} = \boldsymbol{I}, \det \boldsymbol{R} = 1 \right\}.$$
 (2.1)

Consider $\mathbf{v}^b = [u, v, w]^{\mathrm{T}}$ denoting the linear velocity in the Body Reference Frame (BRF), and \mathbf{v}^i representing the linear velocity in the Inertial Reference Frame (IRF). Consequently, the relationship between \mathbf{v}^b and \mathbf{v}^i can be expressed by the equation:

$$\mathbf{v}^i = \mathbf{R}_b^i(\mathbf{\Theta})\mathbf{v}^b. \tag{2.2}$$

Here, Θ comprises the Euler angles—specifically, roll ϕ , pitch θ , and yaw ψ . Subsequently, the rotation matrix can be calculated using Θ as follows:

$$\mathbf{R}_b^i(\Theta) = \mathbf{R}_{z,\psi} \mathbf{R}_{y,\theta} \mathbf{R}_{x,\phi}, \tag{2.3}$$

$$\boldsymbol{R}_{x,\phi} = \begin{bmatrix} 1 & 0 & 0 \\ 0 & \cos\phi & -\sin\phi \\ 0 & \sin\phi & \cos\phi \end{bmatrix}, \boldsymbol{R}_{y,\theta} = \begin{bmatrix} \cos\theta & 0 & \sin\theta \\ 0 & 1 & 0 \\ -\sin\theta & 0 & \cos\theta \end{bmatrix}, \boldsymbol{R}_{z,\psi} = \begin{bmatrix} \cos\psi & -\sin\psi & 0 \\ \sin\psi & \cos\psi & 0 \\ 0 & 0 & 1 \end{bmatrix}.$$
(2.4)

Upon expanding Equation 2.3, the resultant form of the rotation matrix \boldsymbol{R}_b^i is:

$$\mathbf{R}_{b}^{i}(\Theta) = \begin{bmatrix} cos\psi cos\theta & cos\psi sin\theta sin\phi - sin\psi cos\phi & cos\psi cos\theta sin\phi + sin\psi sin\phi \\ sin\psi cos\theta & sin\psi sin\theta cos\phi + cos\psi cos\phi & sin\psi sin\theta cos\phi - cos\psi sin\phi \\ -sin\theta & cos\theta sin\phi & cos\theta cos\phi \end{bmatrix}. \quad (2.5)$$

To convert angular states, consider $\omega^b = [p,q,r]^T$ denoting angular velocity in the Body Reference Frame (BRF) concerning the Inertial Reference Frame (IRF). Subsequently:

$$\dot{\mathbf{\Theta}} = \mathbf{T}(\mathbf{\Theta})\boldsymbol{\omega}^b \tag{2.6}$$

where, $\dot{\Theta} = [\dot{\phi}, \dot{\theta}, \dot{\psi}]$ denotes the Euler angle rate.

The matrix $T(\Theta)$, illustrating the connection between angular states in the BRF and the IRF, can be defined as:

$$\boldsymbol{\omega}^{b} = \begin{bmatrix} \dot{\phi} \\ 0 \\ 0 \end{bmatrix} + \boldsymbol{R}_{x,\phi}^{\mathrm{T}} \begin{bmatrix} 0 \\ \dot{\theta} \\ 0 \end{bmatrix} + \boldsymbol{R}_{x,\phi}^{\mathrm{T}} \boldsymbol{R}_{y,\theta}^{\mathrm{T}} \begin{bmatrix} 0 \\ 0 \\ \dot{\psi} \end{bmatrix}. \tag{2.7}$$

Upon elaborating Equation 2.7, the resulting form of the transformation matrix $T(\Theta)$ is:

$$T(\mathbf{\Theta}) = \begin{bmatrix} 1 & \sin\phi \tan\theta & \cos\phi \tan\theta \\ 0 & \cos\phi & -\sin\phi \\ 0 & \sin\phi/\cos\theta & \cos\phi/\cos\theta \end{bmatrix}, \tag{2.8}$$

$$J(\eta) = \begin{bmatrix} \mathbf{R}_b^i(\mathbf{\Theta}) & \mathbf{0}^{3\times 3}, \\ \mathbf{0}^{3\times 3} & \mathbf{T}(\eta) \end{bmatrix}. \tag{2.9}$$

Consequently, the correlation between the velocity and position of the UUV is ex-

pressed as:

$$\dot{\boldsymbol{\eta}} = \begin{bmatrix} \dot{\mathbf{p}} \\ \dot{\boldsymbol{\Theta}} \end{bmatrix} = \begin{bmatrix} \mathbf{R}_b^i(\boldsymbol{\Theta}) & \mathbf{0}_{3\times 3} \\ \mathbf{0}_{3\times 3} & \mathbf{T}(\boldsymbol{\Theta}) \end{bmatrix} \begin{bmatrix} \mathbf{v}^b \\ \boldsymbol{\omega}^b \end{bmatrix} = \mathbf{J}(\boldsymbol{\eta})\mathbf{v}. \tag{2.10}$$

Here, $\mathbf{p} = [x, y, z]^{\mathrm{T}}$ signifies the linear position of the UUV in the IRF.

2.2.2 Kinetic Model

In order to streamline the derivation of the dynamic equations governing the motion of the UUV, a common and logical approach is to presume the vehicle as a rigid body. This assumption negates the necessity of scrutinizing the interactions among individual mass elements. The comprehensive dynamic model is articulated as:

$$M\dot{v} + C(v)v + D(v)v + g(\eta) = \tau + \tau_{\text{env}}$$
 (2.11)

where M signifies the mass matrix, C(v) represents the Coriolis and centripetal matrix, D(v) stands for the hydrodynamic damping matrix, $g(\eta)$ denotes the vector encompassing gravitational and buoyancy forces, $\tau = [X, Y, Z, K, M, N]^{\mathrm{T}}$ encapsulates the total propulsion forces and moments, and w accounts for the total disturbance. Both M and C(v)v incorporate terms pertaining to both the rigid body and hydrodynamic added mass:

$$\begin{cases}
M = M_{RB} + M_A \\
C(v) = C_{RB}(v) + C_A(v).
\end{cases}$$
(2.12)

Each component within the dynamic model is elaborated upon in subsequent sections.

Rigid-Body Dynamics

The rigid-body dynamics of marine vessels, including the UUV, can be derived through the application of Newtonian mechanics [11]. The rigid-body mass matrix M_{RB} is calculated as:

$$\mathbf{M_{RB}} = \begin{bmatrix} m & 0 & 0 & 0 & mz_g & -my_g \\ 0 & m & 0 & -mz_g & 0 & mx_g \\ 0 & 0 & m & my_g & -mx_g & 0 \\ 0 & -mz_g & my_g & I_x & -I_{xy} & -I_{xz} \\ mz_g & 0 & -mx_g & -I_{yx} & I_y & -I_{yz} \\ -my_g & mx_g & 0 & -I_{zx} & -I_{zy} & I_z \end{bmatrix}.$$
(2.13)

Here, m represents the vehicle's mass, I_x , I_y , and I_z denote the moments of inertia around the x_b , y_b , and z_b axes in the BRF; $r_g = [x_g, y_g, z_g]^{\rm T}$ indicates the position of the center of gravity (CG) relative to the vehicle's center. Given that the BRF origin is situated at the UUV's geometric center, and the vehicle exhibits symmetry in both the xz-plane (port-starboard) and xy-plane (fore-aft), the rigid-body mass matrix can be simplified by assuming $x_g = y_g = 0$ and $I_{xv} = I_{xz} = I_{yz} = 0$. Consequently, Equation 2.14 transforms as:

$$\mathbf{M_{RB}} = \begin{bmatrix} m & 0 & 0 & 0 & mz_g & 0 \\ 0 & m & 0 & -mz_g & 0 & 0 \\ 0 & 0 & m & 0 & 0 & 0 \\ 0 & -mz_g & 0 & I_x & 0 & 0 \\ mz_g & 0 & 0 & 0 & I_y & 0 \\ 0 & 0 & 0 & 0 & 0 & I_z \end{bmatrix}. \tag{2.14}$$

Following this, employing the skew-symmetric cross-product operation on M_{RB} produces the outcome of the rigid-body Coriolis and centripetal matrix $C_{RB}(v)$ as:

$$C_{RB}(\mathbf{v}) = \begin{bmatrix} 0 & 0 & 0 & 0 & mw & -mv \\ 0 & 0 & 0 & -mw & 0 & mu \\ 0 & 0 & 0 & mv & -mu & 0 \\ 0 & mw & -mv & 0 & I_zr & -I_yq \\ -mw & 0 & mu & -I_zr & 0 & I_xp \\ mv & -mu & 0 & I_yq & -I_xp & 0 \end{bmatrix}.$$
(2.15)

Hydrodynamic Forces and Moments

When computing the overall external forces and moments τ , it is imperative to account for hydrodynamics. Key contributors to hydrodynamic forces and moments encompass radiation-induced forces, skin friction damping, wave drift damping, vortex shedding damping, and environmental disturbances. These elements are individually addressed employing the superposition principle.

Hydrodynamic added mass can be viewed as a virtual mass integrated into a system because an accelerating or decelerating body displaces a certain volume of the surrounding fluid as it traverses through it. This concept is derived from Kirchhoff's equation [11]:

$$\mathbf{M_{A}} = - \begin{bmatrix}
X_{\dot{u}} & X_{\dot{v}} & X_{\dot{w}} & X_{\dot{p}} & X_{\dot{q}} & X_{\dot{r}} \\
Y_{\dot{u}} & Y_{\dot{v}} & Y_{\dot{w}} & Y_{\dot{p}} & Y_{\dot{q}} & Y_{\dot{r}} \\
Z_{\dot{u}} & Z_{\dot{v}} & Z_{\dot{w}} & Z_{\dot{p}} & Z_{\dot{q}} & Z_{\dot{r}} \\
K_{\dot{u}} & K_{\dot{v}} & K_{\dot{w}} & K_{\dot{p}} & K_{\dot{q}} & K_{\dot{r}} \\
M_{\dot{u}} & M_{\dot{v}} & M_{\dot{w}} & M_{\dot{p}} & M_{\dot{q}} & M_{\dot{r}} \\
N_{\dot{u}} & N_{\dot{v}} & N_{\dot{w}} & N_{\dot{p}} & N_{\dot{q}} & N_{\dot{r}}
\end{bmatrix} .$$
(2.16)

In an ideal fluid, for a rigid body at rest or moving at a forward speed $U \geqslant 0$, the hydrodynamic system inertia matrix M_A is positive semi-definite. Hydrodynamic coefficients are defined as the partial derivatives of the added mass force with respect to the corresponding acceleration. For instance, the added mass force $Z_{\dot{u}}$ along the z-axis due to the acceleration \dot{u} is denoted as $Z_{\dot{u}} = \frac{\partial Z}{\partial \dot{u}}$.

Given that in most practical scenarios the non-diagonal elements of M_A are considerably smaller than the diagonal elements [11], the off-diagonal terms of M_A can be disregarded. Consequently, M_A can be simplified as:

$$\mathbf{M_A} = - \begin{bmatrix}
X_{\dot{u}} & 0 & 0 & 0 & 0 & 0 \\
0 & Y_{\dot{v}} & 0 & 0 & 0 & 0 \\
0 & 0 & Z_{\dot{w}} & 0 & 0 & 0 \\
0 & 0 & 0 & K_{\dot{p}} & 0 & 0 \\
0 & 0 & 0 & 0 & M_{\dot{q}} & 0 \\
0 & 0 & 0 & 0 & 0 & N_{\dot{r}}
\end{bmatrix}.$$
(2.17)

Thus, the computation of the nonlinear hydrodynamic Coriolis and centripetal matrix $C_A(v)$ can be performed as:

$$C_{\mathbf{A}}(\mathbf{v}) = \begin{bmatrix} 0 & 0 & 0 & 0 & z_{\dot{w}}w & 0 \\ 0 & 0 & 0 & -z_{\dot{w}}w & 0 & -X_{\dot{u}}u \\ 0 & 0 & 0 & -Y_{\dot{v}}v & X_{\dot{u}}u & 0 \\ 0 & -z_{\dot{w}}w & Y_{\dot{v}}v & 0 & -N_{\dot{r}}r & M_{\dot{q}}q \\ z_{\dot{w}}w & 0 & -X_{\dot{u}}u & N_{\dot{r}}r & 0 & -K_{\dot{p}}p \\ -Y_{\dot{v}}v & X_{\dot{u}}u & 0 & -M_{\dot{q}}q & K_{\dot{p}}p & 0 \end{bmatrix}.$$
 (2.18)

Hydrodynamic damping in marine vessels primarily arises from various factors as explained by [11]:

• Potential Damping: This type of damping involves the interaction of damping and restoring forces and moments when a body oscillates at the wave excitation frequency without encountering incident waves. The radiation-induced damping term is commonly known as linear frequency-dependent potential damping.

- Skin Friction: Arising from laminar boundary layer theory, the linear frequency-dependent skin friction is significant for the low-frequency motion of marine vessels.

 Additionally, turbulent boundary layers contribute to high-frequency skin friction.
- Wave Drift Damping: Present as added resistance for surface vessels moving through waves, wave drift damping is rooted in second-order wave theory. It notably affects surge in higher sea states due to wave drift forces being proportional to the square of the significant wave height. In comparison, sway and yaw experience relatively minor wave drift damping compared to vortex shedding.
- Damping Due to Vortex Shedding: In a viscous fluid, non-conservative frictional forces lead to interference drag, stemming from the shedding of vortex sheets at sharp edges.

Potential damping and wave drift damping effects are typically disregarded for underwater vehicles. These diverse damping components contribute to both linear and quadratic damping terms:

$$D(v) = D_L + D_{NL}(v), \tag{2.19}$$

here, D_L represents the linear damping component induced by skin friction, while D_{NL} denotes the nonlinear damping matrix arising from quadratic damping and higher-order effects. The damping matrix is diagonalized due to decoupling, leading to the formulation of the linear and quadratic damping matrices as described in Equation 2.20 and Equation 2.21 respectively:

$$\mathbf{D_L} = -\operatorname{diag}[X_u, Y_v, Z_w, K_p, M_q, N_r], \qquad (2.20)$$

$$\mathbf{D_{NL}}(\mathbf{v}) = -\operatorname{diag}\left[X_{u|u|}|u|, Y_{v|v|}|v|, Z_{w|w|}|w|, K_{p|p|}|p|, M_{q|q|}|q|, N_{r|r|}|r|\right]. \tag{2.21}$$

Consequently, the complete hydrodynamic damping term is expressed as:

$$D(v) = D_{L} + D_{NL}(v)$$

$$= -\operatorname{diag}[X_{u}, Y_{v}, Z_{w}, K_{p}, M_{q}, N_{r}]$$

$$-\operatorname{diag}[X_{u|u|}|u|, Y_{v|v|}|v|, Z_{w|w|}|w|, K_{p|p|}|p|, M_{q|q|}|q|, N_{r|r|}|r|].$$
(2.22)

Hydrostatics

Archimedes [12] established the foundational principles of fluid statics, which form the basis of modern hydrostatics. In hydrostatic terms, the gravitational and buoyancy forces are termed restoring forces, akin to the spring forces in a mass-damper-spring system. With m representing the mass of the UUV, g denoting the acceleration due to gravity, ρ standing for the water density, and ∇ representing the volume of fluid displaced by the UUV, the weight of the UUV can be articulated as:

$$W = mq. (2.23)$$

Meanwhile, the buoyancy force B here is expressed as:

$$B = \rho g \nabla. \tag{2.24}$$

Assuming the centre of buoyancy (CB) of the UUV is located at $r_b = [x_b, y_b, z_b]^T$, if we consider the center of the vehicle's body frame to be positioned at the CB, then r_b is defined as:

$$r_b = [0, 0, 0]^T. (2.25)$$

Since the vehicle has symmetry in the xz-plane and xy-plane, the position of the CG

of the vehicle r_g becomes:

$$r_g = \begin{bmatrix} x_g & y_g & z_g \end{bmatrix}^T = [0, 0, z_g]^T.$$
 (2.26)

Then the overall restoring force vector $g(\eta)$ can be calculated using Euler angle transformation as:

$$g(\eta) = \begin{bmatrix} (W - B)\sin\theta \\ -(W - B)\cos\theta\sin\phi \\ -(W - B)\cos\theta\cos\phi \\ z_gW\cos\theta\sin\phi \\ z_gW\sin\theta \\ 0 \end{bmatrix}. \tag{2.27}$$

Propeller Model and Control Allocation

A practical model of a propeller is examined within the dynamics of an Unmanned Underwater Vehicle (UUV). The UUV can be managed in four degrees of freedom (DOF): forward/backward movement, side-to-side movement, vertical movement, and rotation. Consequently, the control commands $\boldsymbol{u} = [u_1, u_2, u_3, u_4]^T$ are established, correlating to the forces and moments in the UUV's various movement dimensions. These control commands are then distributed among the propellers using a control allocation matrix. In the context of this study, focusing on the blueROV2, the thrust vector $\boldsymbol{t} = [t_1, t_2, t_3, t_4, t_5, t_6]^T$ is computed as:

$$t = Au = \begin{bmatrix} -1 & 1 & 0 & 1 \\ -1 & -1 & 0 & -1 \\ 1 & 1 & 0 & -1 \\ 1 & -1 & 0 & 1 \\ 0 & 0 & -1 & 0 \\ 0 & 0 & -1 & 0 \end{bmatrix} u.$$
 (2.28)

In this configuration, t represents the combined thrust generated by all propellers. The arrangement consists of six propellers as illustrated in Figure 2.4. The blue propellers spin in a clockwise direction, while the green propellers spin counterclockwise. A red arrow denotes the positive surge orientation.

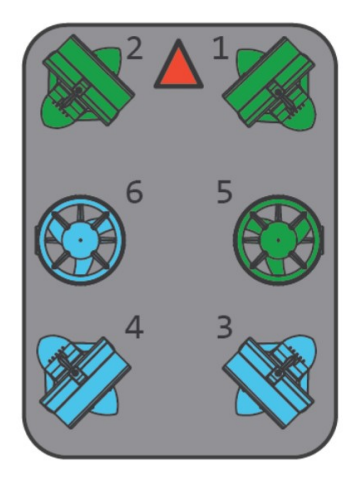


Figure 2.4: The propeller configuration of the BlueROV2, including two vertical propellers and four horizontal propellers.

Utilizing the thrust force of each individual propeller, the total force and moment exerted on the UUV can be computed using a propulsion matrix derived from the geometry of the blueROV2 as follows:

$$\tau = Kt \tag{2.29}$$

To determine the forces and moments generated by propeller 1 for computing the propulsion matrix, where l_{x1} represents the distance between the center of propeller 1 and the CG in the x_b direction, and t_{x1} is the force projection in the x_b direction, the calculations are as follows:

$$\tau_{1} = \begin{bmatrix} t_{x1} \\ t_{y1} \\ t_{z1} \\ t_{z1}l_{y1} - t_{y1}l_{z1} \\ t_{x1}l_{z1} - t_{z1}l_{x1} \\ t_{y1}l_{x1} - t_{x1}l_{y1} \end{bmatrix} = \begin{bmatrix} t_{1}\cos\alpha \\ -t_{1}\sin\alpha \\ 0 \\ t_{1}\sin\alpha \cdot l_{z1} \\ t_{1}\cos\alpha \cdot l_{z1} \\ t_{1}(-\sin\alpha \cdot l_{x1} - \cos\alpha \cdot l_{y1}) \end{bmatrix}$$

$$= \begin{bmatrix} \cos\alpha \\ -\sin\alpha \\ 0 \\ \sin\alpha \cdot l_{z1} \\ \cos\alpha \cdot l_{z1} \\ -\sin\alpha \cdot l_{x1} - \cos\alpha \cdot l_{y1} \end{bmatrix} t_{1}$$

$$(2.30)$$

Given that α represents the orientation of the propeller, with the specified values $\alpha = \pi/4$ and $l_{x1} = 0.156$, $l_{y1} = 0.111$, $l_{z1} = 0.072$ for propeller 1, the initial column in the propulsion matrix, denoted as K, can be determined. Subsequent columns can be computed similarly, leading to the complete propulsion matrix as follows:

$$\boldsymbol{K} = \begin{bmatrix} 0.707 & 0.707 & -0.707 & -0.707 & 0 & 0 \\ -0.707 & 0.707 & -0.707 & 0.707 & 0 & 0 \\ 0 & 0 & 0 & 0 & 1 & 1 \\ 0.051 & -0.051 & 0.051 & -0.051 & 0.111 & -0.111 \\ 0.051 & 0.051 & -0.051 & -0.051 & 0.002 & -0.002 \\ -0.167 & 0.167 & 0.175 & -0.175 & 0 & 0 \end{bmatrix}.$$
(2.31)

In practice, the signals sent to each propeller are in the form of Pulse Width Modulation (PWM) signals. The Figure 2.5 is provided by the manufacturer, which specifies the relationship between the PWM input and the thrust is not linear.

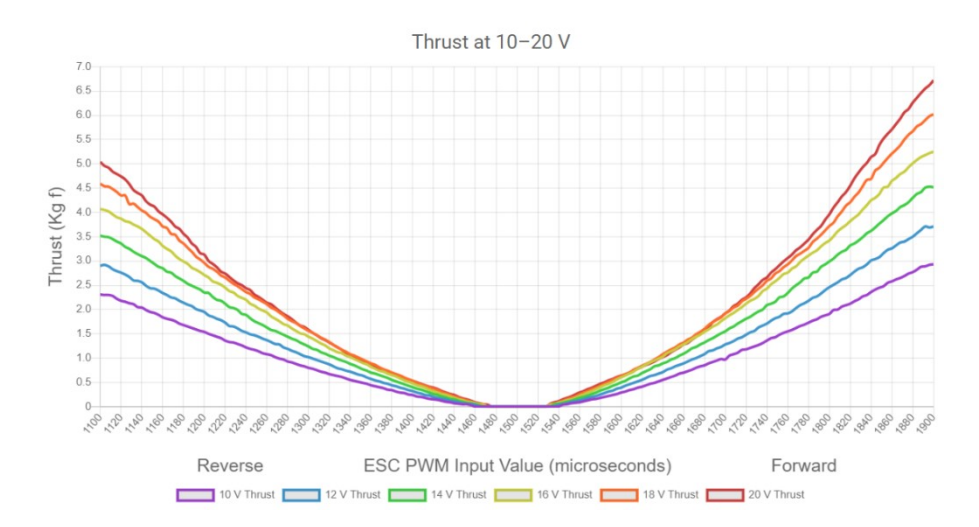


Figure 2.5: Thrust polynomial fitting based on PWM input value within 10-20 V.

Thus, the relationship between thrusts and PWM signal is investigated by applying fourth order polynomial fitting:

$$t_{kgf} = -6.5453 \times 10^{-12} X_{pwm}^4 + 7.6349 \times 10^{-8} X_{pwm}^3 - 2.5053 \times 10^{-4} X_{pwm}^2$$

$$+ 0.3312 X_{pwm} - 157.6016$$
(2.32)

where the t_{kgf} is the thrust in unit of kgf, and X_{pwm} is the PWM input. The thrusts from the datasheet and the thrusts calculated based on polynomial fitting are shown as Figure 2.6.

2.2.3 UUV Model for Motion Control

For achieving motion control of the UUV, the system state is defined as $\boldsymbol{x} = [\boldsymbol{\eta}^T, \boldsymbol{v}^T]^T$. From the Equation 2.10 and Equation 2.11, the general form of the UUV is obtained as:

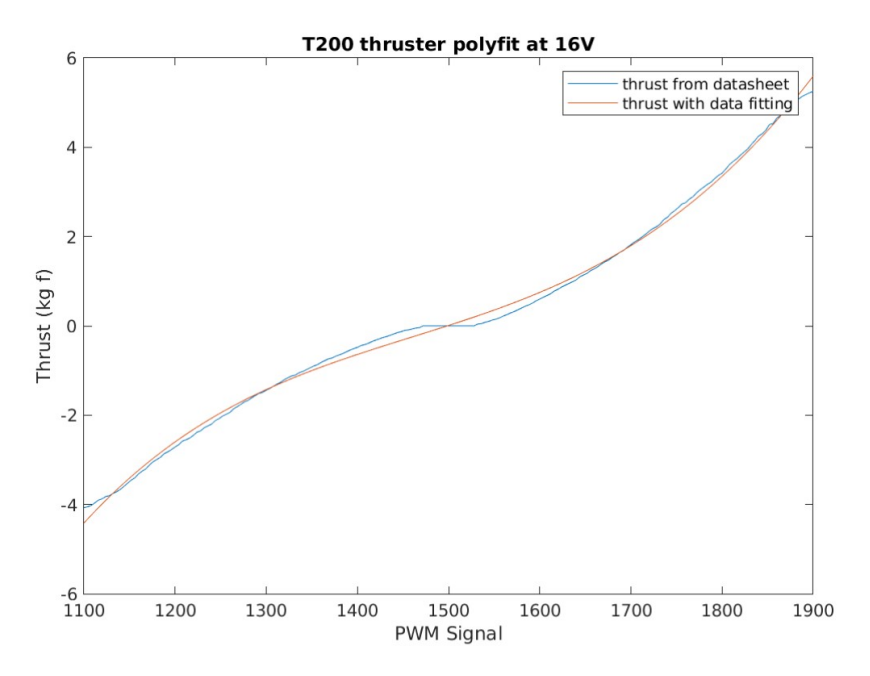


Figure 2.6: Thrust polynomial fitting results through fourth order fitting.

$$\dot{\boldsymbol{x}} = \begin{bmatrix} \dot{\boldsymbol{\eta}} \\ \dot{\boldsymbol{v}} \end{bmatrix} = f(\boldsymbol{x}, \boldsymbol{\tau}, \boldsymbol{w}, t)$$

$$= \begin{bmatrix} J(\boldsymbol{\eta})\boldsymbol{v} \\ M^{-1} \left[\boldsymbol{\tau} + \boldsymbol{\tau}_{env} - \boldsymbol{C}(\boldsymbol{v})\boldsymbol{v} - \boldsymbol{D}(\boldsymbol{v})\boldsymbol{v} - \boldsymbol{g}(\boldsymbol{\eta}) \right] \end{bmatrix}$$
(2.33)

where M and C(v)v contain both rigid body term and hydrodynamic added mass term:

$$\begin{cases}
M = M_{RB} + M_A \\
C(v) = C_{RB}(v) + C_A(v)
\end{cases}$$
(2.34)

Chapter 3

Disturbance Observer-Based Model

Predictive Control

This chapter offers a comprehensive overview of a reliable DOBMPC approach utilizing the proposed EAOB. It includes a literature review of related works, the methodology employed, results of control performance and observation, and concluding remarks. This chapter has been previously published as part of author's work in the [9].

3.1 Literature Review

The complexities inherent in developing control systems for UUVs arise from their highly nonlinear dynamics, the uncertainties in their parameters and the unpredictable disturbances present in their operating environments. To address these challenges, many control methods have been explored within the realm of UUV operations. Among these strategies, the PID controller stands out as a widely employed mechanism in UUV control frameworks [13]. Noteworthy for its capacity to adeptly navigate parameter uncertainties, PID control distinguishes itself from other techniques by its reliance on real-time error feedback rather than precise system models. This inherent adaptability empowers the

PID controller to adjust control outputs dynamically, thereby accommodating variations and uncertainties in system parameters, consequently ensuring robust operational performance. The application of PID controllers in UUVs spans diverse variants, including the fractional-order PID controller tailored to optimize parameters amidst uncertainties [14], the adaptive fuzzy PID controller offering resilience against external disturbances [4], and the intelligent-PID with feedforward mechanism, augmenting stability [15]. However, PID controllers are inherently linear controllers and may struggle to effectively control highly nonlinear UUV systems. UUV dynamics can exhibit complex nonlinear behaviors that may not be adequately addressed by a PID controller's linear control scheme.

Besides of PID methods, SMC emerges as another popular control approach in UUV motion regulation [16]. Renowned for its effectiveness in managing systems characterized by uncertainties, disturbances, and nonlinearities, SMC has been leveraged in devising a dual closed-loop integral SMC methodology tailored for controlling underactuated UUVs [5]. This technique adeptly addresses the intricate nonlinear and coupled dynamics of the vehicle, rendering it apt for navigating three-dimensional underactuated scenarios. Moreover, a sliding mode-based fault-tolerant control mechanism integrated with thrust allocation has been proposed to mitigate steady errors arising from thruster faults [17]. Nonetheless, the chattering phenomenon inherent to SMC, stemming from its discontinuous control law under high-speed UUV maneuvers, poses challenges by compromising accuracy and inducing energy losses.

MPC, a control method entailing the recursive solution of an OCP over a finite horizon to determine control actions [18]. This methodology ensures consistent consideration of system constraints throughout the control process, thereby garnering considerable interest in the domain of marine robotics for its adeptness in managing control constraints, variation bounds, and state restrictions. The integration of MPC in marine vessels for dynamic positioning, as evidenced in [19], showcases its efficacy in distributing force generation over defined time intervals and facilitating motion planning based on varying

configurations of rotatable thrusters. Noteworthily, NMPC has been tailored to enable an AUV to track predefined trajectories within the water column [20], highlighting the potential for real-time MPC control leveraging in situ estimated water current profiles. Furthermore, the advent of Lyapunov-based MPC methodologies, as exemplified in [21], ensures closed-loop stability, with the robustness of NMPC validated through experimental trials in water tanks capable of simulating directional ocean currents [22]. These studies underpin the advantages of MPC in UUV motion control, elucidating its efficacy through a blend of numerical simulations and experimental validations.

While MPC has demonstrated effectiveness in controlling UUVs, addressing parametric uncertainties and environmental disturbances remains a critical consideration. DOBC is a control technique devised to tackle the challenges posed by environmental disturbances within a control system. DOBC involves estimating and compensating for disturbances to bolster overall system performance and robustness, encompassing unmodeled dynamics and environmental disturbances as part of its domain. Notably, one of the advantages of DOBC is that it ensures the performance of the outer-loop controller remains intact even when disturbances are estimated within the inner loop.

In 2018, A Nonlinear Disturbance Observer (NDO) was developed and integrated into a nonsingular fast terminal sliding mode control scheme for trajectory tracking of an underactuated UUV [23]. This integration ensures finite-time convergence and demonstrates enhanced immunity to external disturbances. In another study, a disturbance observer was incorporated into fuzzy adapted S-Surface control to enhance robustness against unmodeled disturbances [24]. A 2019 study introduced a modified constrained controller that combines a computed-torque controller with a newly designed NDO for improved performance [25]. This modification boosts the accuracy of disturbance compensation by refining the evaluation function of the traditional H_{∞} controller while considering control input constraints.

Recently, MPC based on ADRC was proposed for motion control of an AUV [7].

This approach incorporates a discrete extended state observer to estimate disturbances and applies feedback control to compensate for them. By amalgamating the strengths of MPC and DOBC, this controller structure adeptly manages parametric uncertainties and external disturbances within the inner loop while addressing system constraints in the outer loop. Hence, advancing a robust disturbance observer resilient to measurement noise could pave the way for a viable and efficient UUV control system.

Driven by the considerations mentioned earlier, an EAOB has been devised in this study, leveraging the extended Extended Kalman Filter (EKF) to merge with MPC, forming the DOBMPC. The key innovation of the developed EAOB lies in its ability to estimate disturbances amidst the presence of measurement noise. Moreover, the unmodeled parameter within the MPC's predictive model is assimilated into the disturbance term, effectively tackling the challenge of parametric uncertainty. In contrast to the traditional method of compensating estimated disturbances directly into control inputs, the estimated disturbances are integrated into the MPC's predictive model and updated at each time increment. This approach enables the MPC to craft an optimal control strategy while accommodating disturbances.

To optimize computational efficiency during the application of MPC in practical scenarios, it is essential to streamline computational processes. This study achieves computational efficiency improvements by employing ACADOS. Nonetheless, there exist alternative methodologies suitable for real-time integration of MPC. In 2020, a novel category of condensing-based MPC iteration strategies was introduced, showcasing asymptotic stability and ensuring crucial constraint adherence within the closed-loop system, regardless of the number of Newton updates performed. Another iteration scheme aimed at reducing computational load for constrained discrete-time linear systems was proposed, specifically tailored for moving horizon estimation-based output feedback MPC. Furthermore, a resilient early termination MPC strategy was recently developed, leveraging barrier functions and continuous-time primal-dual gradient flow techniques. Findings indicated that

this approach provides a suboptimal yet viable and efficient solution when early termination is activated. Exploring these alternate algorithms holds promise for enhancing the MPC implementation, offering diverse avenues to boost computational efficiency.

3.2 Methodology

In this section, it outlines the methodology behind the proposed DOBMPC, a type of AMPC employed in this project. The DOBMPC is formulated based on the EAOB. Consequently, this section covers the design of the EAOB, stability analysis of the observer, and the implementation of MPC.

In the realm of control system design, it is common practice to adopt the principle of superposition when factoring in environmental disturbances τ_{env} , such as wave and current disturbances [11]. These disturbances encompass unmodeled dynamics $\Delta \tau$, which encompass uncertainties linked to rigid-body parameters (for instance, inertia and mass properties) and hydrodynamic parameters (like hydrodynamic damping forces) that are challenging to precisely determine. This principle dictates that all disturbance sources are aggregated and incorporated on the right-hand side of Equation 2.33 as the disturbance term $\mathbf{w} = [X_w, Y_w, Z_w, K_w, M_w, N_w]^T$:

$$\boldsymbol{w} = \boldsymbol{\tau}_{\text{env}} + \Delta \tau. \tag{3.1}$$

Assumption 1 It is assumed that the influence of environmental disturbances (τ_{env}) , like oceanic waves and currents, and the unmodeled dynamics $(\Delta \tau)$, are constrained, specifically by $|\tau_{env}| \leq \overline{\tau_1}$ and $|\Delta \tau| \leq \overline{\tau_2}$. Here, $\overline{\tau_1}$ and $\overline{\tau_2}$ denote unspecified positive constants of estimations. Consequently, the overall disturbance \boldsymbol{w} is capped by the cumulative value of these thresholds, denoted as $|\boldsymbol{w}| \leq \overline{\tau_1} + \overline{\tau_2}$.

Assumption 2 The total disturbance w is assumed to be a slowly time-varying signal.

Consequently, the internal disturbance model can be formulated as:

$$\begin{cases}
\mathbf{w} = \mathbf{M}\dot{\mathbf{v}} + \mathbf{C}(\mathbf{v})\mathbf{v} + \mathbf{D}(\mathbf{v})\mathbf{v} + \mathbf{g}(\mathbf{\eta}) - \mathbf{\tau} \\
\dot{\mathbf{w}} = 0.
\end{cases}$$
(3.2)

3.2.1 Observer Design

When employing an EKF to devise a disturbance observer for offsetting unpredictable uncertainties, the disturbance term w is regarded as system states in conjunction with the position η and velocity v.

In practical scenarios, it is common for modeled systems to exhibit continuous-time dynamics, whereas measurements are acquired at discrete intervals. To tackle this challenge, the Continuous-Discrete Extended Kalman Filter (CD-EKF) is utilized for constructing the EAOB. The CD-EKF integrates continuous and discrete dynamics into the estimation procedure, akin to the standard EKF but with the added capability of accommodating discrete dynamics. Continuous dynamics are typically defined by differential equations, while discrete dynamics are characterized by distinction equations. During the prediction phase of the CD-EKF, the continuous dynamics are discretized by forward integration in time using numerical integration methods, effectively capturing the system's continuous progression between measurement updates. In the update phase, the CD-EKF merges the discrete-time measurements to rectify and refine the state estimation. By seamlessly amalgamating continuous and discrete dynamics within the estimation framework, the CD-EKF enhances accuracy and resilience in estimating the state variables of systems with mixed dynamics. Thus, the system process is delineated as a continuous-time model, while discrete-time measurements are employed. The system process model can

be reconstructed as:

$$\dot{\boldsymbol{x}_{ob}}(t) = f(\boldsymbol{x}(t), \boldsymbol{\tau}(t), \boldsymbol{w}(t)) + \boldsymbol{W}(t) \quad \boldsymbol{W}(t) \sim \mathcal{N}(0, \boldsymbol{Q}(t)).$$
 (3.3)

where the observer system states are denoted as $\boldsymbol{x_{ob}} = [\boldsymbol{\eta}; \boldsymbol{v}; \boldsymbol{w}]$, where $\boldsymbol{W}(t)$ signifies the process noise assumed to be zero-mean Gaussian noise with covariance $\boldsymbol{Q}(t)$. The function $f(\cdot)$ pertains to the nonlinear system process model, and t denotes time continuously. Consequently, all functions within the system process model are specified in continuous time.

Hence, the system process model can be structured according to the UUV model in Equation 2.33:

$$f(\boldsymbol{x}, \boldsymbol{\tau}, \boldsymbol{w}) = \begin{bmatrix} \boldsymbol{J}(\boldsymbol{\eta})\boldsymbol{v} \\ (\boldsymbol{M})^{-1}[\boldsymbol{\tau} + \boldsymbol{w} - \boldsymbol{C}(\boldsymbol{v})\boldsymbol{v} - \boldsymbol{D}(\boldsymbol{v})\boldsymbol{v} - \boldsymbol{g}(\boldsymbol{\eta})] \\ \dot{\boldsymbol{w}} \end{bmatrix}$$
(3.4)

The measurement states encompass the position η , velocity v, and propulsion forces and moments τ . Therefore, the discrete-time measurement model is formulated as:

$$\boldsymbol{z}_{k} = h\left(\boldsymbol{x}_{ob,k}\right) + \boldsymbol{V}_{k} \quad \boldsymbol{V}_{k} \sim \mathcal{N}\left(0, \boldsymbol{R}_{k}\right)$$
 (3.5)

In this context, the measurement states are represented as $\mathbf{z} = [\boldsymbol{\eta}; \boldsymbol{v}; \boldsymbol{\tau}]$, where \boldsymbol{V}_k signifies the measurement noise assumed to be zero-mean Gaussian noise with covariance \boldsymbol{R}_k . The function $h(\cdot)$ relates to the nonlinear measurement model that establishes the connection between the system states and the measurements acquired from sensors, while k denotes time discretely. Therefore, all functions within the measurement model are specified in discrete time. The initial 12 terms of the measurement model correspond identically to the system process model, and the $\boldsymbol{\tau}$ can be computed based on the disturbance term \boldsymbol{w}

as:

$$\tau = M\dot{v} + C(v)v + D(v)v + g(\eta) - w. \tag{3.6}$$

The accurate estimation of solutions heavily relies on designing the noise covariance matrices for the system process Q(t) and measurements R_k . One method to create Q(t) involves utilizing the Piecewise White Noise Model (PWNN) model. This stochastic model allows for representing varying noise characteristics across different time intervals or regions. By integrating PWNN, the EKF can more accurately capture the time-varying dynamics of the system. This proves especially beneficial for systems with changing or non-stationary noise traits. The formula for calculating the system process noise covariance Q(t) based on PWNN is as follows:

$$\mathbf{Q}(t) = \mathbb{E}\left[\Gamma W(t)W(t)\Gamma^{\top}\right] = \Gamma \sigma^{2}\Gamma^{\top}.$$
(3.7)

where $\Gamma = [\Delta t^2/2, \Delta t, \Delta t]^T$ is the noise gain of the system, Δt is the sampling time step, and σ^2 represents the variance of the white noise process. The covariance of the measurement noise \mathbf{R}_k is also dependent on the sampling time step Δt , which is defined as:

$$\mathbf{R}_k = diag[\Delta t, \Delta t, \Delta t]. \tag{3.8}$$

To adapt the real-world implementation, the matrix \mathbf{R}_k can be further fine-tuned according to the specific sensors employed. For instance, the accelerometer and gyroscope are commonly employed for state measurement, but they often introduce unavoidable noise into the measurements. Consequently, in such cases, it is crucial to carefully determine the measurement noise matrix \mathbf{R}_k . Numerous studies have been conducted in this area. In 2021, an experimental approach was proposed to analyze the impact of different weightings of matrix $\mathbf{Q}(t)$ and \mathbf{R}_k on state estimation derived from the accelerometer and gyroscope [26]. In addition, a study also developed a dynamic noise model for adaptive filtering of the gyroscope [27]. This work introduced the dynamic Allan variance, which

utilized a novel truncation window based on entropy features to construct the noise model. Additionally, an adaptive Kalman filter was designed to accommodate practical system and computational environments. Furthermore, a disturbance observer with adaptation laws has been developed based on the Generalized Super-Twisting Algorithm [28]. This allows the observer to be auto-tuned, improving robustness to both external disturbances and model uncertainties.

The matrix Q(t) is used to model the uncertainty and variability in the system dynamics. By adjusting the Q(t), it can control the level of confidence the observer has in the predicted state estimates. Meanwhile, the matrix R_k captures the uncertainty associated with the sensor measurements. Consequently, the tuning of Q(t) and R_k determines the weighting between the system model and the measurements. As the current work is being conducted in simulation, where higher measurement accuracy is present, further adjusting R_k allows for greater reliance on measurements:

$$\mathbf{R}_k = diag[\Delta t^2/2, \Delta t^2/2, \Delta t^2/2]. \tag{3.9}$$

The system process model $f(x, \tau, w)$ and the measurement model $h(x_{ob})$ can be linearized by taking the partial derivatives of each to evaluate the state transition matrix \mathbf{F} and the measurement matrix \mathbf{H} at each operating point with Jacobian matrix. Equation 3.10 provides the state transition matrix \mathbf{F} that captures the connection between the current state and the subsequent predicted state in a dynamic system. This matrix is derived using continuous-time t as a basis. The measurement matrix, denoted as \mathbf{H} , establishes the connection between sensor measurements and the predicted system state, as expressed in Equation 3.11, with consideration for discrete-time k.

$$\boldsymbol{F}(t) = \frac{\partial f}{\partial \boldsymbol{x}_{ob}} \bigg|_{\hat{\boldsymbol{x}}(t), \boldsymbol{\tau}(t), \hat{\boldsymbol{w}}(t)}$$
(3.10)

$$\boldsymbol{H}_{k} = \frac{\partial h}{\partial \boldsymbol{x}_{ob}} \bigg|_{\hat{\boldsymbol{x}}_{ob,k|k-1}}$$
(3.11)

Denote the three elements in the second row of matrix F(t) as $F_{21}(t)$, $F_{22}(t)$, and $F_{23}(t)$. Therefore

$$F_{21}(t) = -\mathbf{M}^{-1} \left(\frac{\partial \mathbf{M}}{\partial \hat{\boldsymbol{\eta}}} \dot{\hat{\boldsymbol{v}}} + \frac{\partial \mathbf{C}(\hat{\boldsymbol{v}}) \hat{\boldsymbol{v}}}{\partial \hat{\boldsymbol{\eta}}} + \frac{\partial \mathbf{D}(\hat{\boldsymbol{v}}) \hat{\boldsymbol{v}}}{\partial \hat{\boldsymbol{\eta}}} + \frac{\partial \mathbf{g}(\hat{\boldsymbol{\eta}})}{\partial \hat{\boldsymbol{\eta}}} \right),$$

$$F_{22}(t) = -\mathbf{M}^{-1} \left(\frac{\partial \mathbf{C}(\hat{\boldsymbol{v}}) \hat{\mathbf{v}}}{\partial \hat{\boldsymbol{v}}} + \frac{\partial \mathbf{D}(\hat{\boldsymbol{v}}) \hat{\boldsymbol{v}}}{\partial \hat{\boldsymbol{v}}} \right),$$

$$F_{23}(t) = \mathbf{M}^{-1}.$$
(3.12)

The CD-EKF is a recursive estimation algorithm, where the main procedure can be divided into prediction and update parts. Before starting the recursion, an initialization step is performed based on the first measurement:

$$\hat{\boldsymbol{x}}_{ob}(t_0) = E\left[\boldsymbol{x}_{ob}(t_0)\right], \boldsymbol{P}(t_0) = \operatorname{Var}\left[\boldsymbol{x}_{ob}(t_0)\right]. \tag{3.13}$$

In the prediction part, it predicts the state estimate $\hat{\boldsymbol{x}}_{ob,k|k-1} = \hat{\boldsymbol{x}}_{ob}(t_k)$ based on the previous state estimate and the system dynamics. Then the error covariance matrix $\boldsymbol{P}_{k|k-1} = \boldsymbol{P}(t_k)$ can be calculated based on the state transition matrix \boldsymbol{F} . The prediction part is shown as follows:

solve
$$\begin{cases} \dot{\hat{\boldsymbol{x}}}_{ob}(t) = f(\hat{\boldsymbol{x}}_{ob}(t), \boldsymbol{\tau}(t)) \\ \dot{\boldsymbol{P}}(t) = \boldsymbol{F}(t)\boldsymbol{P}(t) + \boldsymbol{P}(t)\boldsymbol{F}(t)^{T} + \boldsymbol{Q}(t) \end{cases}$$
with
$$\begin{cases} \hat{\boldsymbol{x}}_{ob}(t_{k-1}) = \hat{\boldsymbol{x}}_{ob,k-1|k-1} \\ \boldsymbol{P}(t_{k-1}) = \boldsymbol{P}_{k-1|k-1} \end{cases} \Rightarrow \begin{cases} \hat{\boldsymbol{x}}_{ob,k|k-1} = \hat{\boldsymbol{x}}_{ob}(t_{k}) \\ \boldsymbol{P}_{k|k-1} = \boldsymbol{P}(t_{k}). \end{cases}$$
(3.14)

The prediction step consists of both continuous-time and discrete-time components. The first equation, $\dot{\hat{x}}_{ob}(t) = f(\hat{x}_{ob}(t), \tau(t))$, represents the continuous-time dynamics of the system. It describes how the estimated state \hat{x}_{ob} evolves over time based on

the current estimated state and the total propulsion force and moments τ . The second equation, $\dot{\boldsymbol{P}}(t) = \boldsymbol{F}(t)\boldsymbol{P}(t) + \boldsymbol{P}(t)\boldsymbol{F}(t)^T + \boldsymbol{Q}(t)$, represents the continuous-time evolution of the error covariance matrix \boldsymbol{P} . It captures how the uncertainty in the estimated state evolves over time, taking into account the system's dynamics represented by the matrix \boldsymbol{F} and the process noise covariance matrix \boldsymbol{Q} . The discretization occurs implicitly between the time steps t_{k-1} and t_k . The initial conditions for the discrete-time updates are set based on the estimated state and error covariance matrix at time t_{k-1} , denoted by $\hat{\boldsymbol{x}}_{k-1|k-1}$ and $\boldsymbol{P}_{k-1|k-1}$, respectively. These initial values are then used to compute the updated estimates $\hat{\boldsymbol{x}}_{ob,k|k-1}$ and $\boldsymbol{P}_{k|k-1}$ at time t_k .

Therefore, in Equation 3.14, a numerical integration method should be applied for discretization of continuous-time system process model. The numerical integration method used for discretization here is the Fourth-Order Runge-Kutta (RK4) method.

In the update part, it calculates the measurement residual $\hat{y}_{k|k}$ with current measurements z(k) and measurement model. Then the Kalman Gain K_k at time k can be determined based in the predicted error covariance matrix $P_{k|k-1}$ and linearized measurement matrix H_k . Finally, it updates the state estimate $\hat{x}_{ob,k|k}$ based on the predicted state estimate $\hat{x}_{ob,k|k-1}$ and the Kalman Gain K_k , and recalculate the error covariance matrix $P_{k|k}$ based on Kalman Gain K_k and the linearized measurement model H_k . The following equations express the procedure in EKF's update part

$$\hat{\boldsymbol{y}}_{k|k} = (\boldsymbol{z}_k - h(\hat{\boldsymbol{x}}_{ob,k|k-1}))$$

$$\boldsymbol{K}_k = \boldsymbol{P}_{k|k-1} \boldsymbol{H}_k^T (\boldsymbol{H}_k \boldsymbol{P}_{k|k-1} \boldsymbol{H}_k^T + \boldsymbol{R}_k)^{-1}$$

$$\hat{\boldsymbol{x}}_{ob,k|k} = \hat{\boldsymbol{x}}_{ob,k|k-1} + \boldsymbol{K}_k \hat{\boldsymbol{y}}_{k|k}$$

$$\boldsymbol{P}_{k|k} = (\boldsymbol{I} - \boldsymbol{K}_k \boldsymbol{H}_k) \boldsymbol{P}_{k|k-1}.$$
(3.15)

The equation in the EKF update part is formulated in discrete time. The time step at which the equation is evaluated is denoted by k. The notation $k \mid k$ signifies that the variable or state being considered is at time step k. On the other hand, $k \mid k-1$ refers to

the estimation or prediction at time step k based on the information available up to the previous time step, which is k-1.

Therefore, the state estimation $\hat{\boldsymbol{x}}_{ob} = [\hat{\boldsymbol{\eta}}; \hat{\boldsymbol{v}}; \hat{\boldsymbol{w}}]$ can be obtained.

3.2.2 Stability Analysis

The system process model Equation 3.4 can be extended as:

$$\dot{\boldsymbol{x}}_{ob} = f(\boldsymbol{x}, \boldsymbol{\tau}, \boldsymbol{w}) + \boldsymbol{G}\boldsymbol{\xi}_{\boldsymbol{x}} \\
= \begin{bmatrix} \boldsymbol{J}(\boldsymbol{\eta})\boldsymbol{v} \\ (\boldsymbol{M})^{-1}[\boldsymbol{\tau} + \boldsymbol{w} - \boldsymbol{C}(\boldsymbol{v})\boldsymbol{v} - \boldsymbol{D}(\boldsymbol{v})\boldsymbol{v} - \boldsymbol{g}(\boldsymbol{\eta})] \\ \dot{\boldsymbol{w}} \end{bmatrix} + \boldsymbol{G} \begin{bmatrix} \boldsymbol{\xi}_{\boldsymbol{\eta}} \\ \boldsymbol{\xi}_{\boldsymbol{v}} \\ \boldsymbol{\xi}_{\boldsymbol{w}} \end{bmatrix}, \quad (3.16)$$

$$\boldsymbol{Y} = \boldsymbol{H}\boldsymbol{x}_{ob} + \boldsymbol{V}_{k}$$

where Y is the output of the system, G is a unit matrix, ξ_{η}, ξ_{v} and ξ_{w} represent the process noises of system states $[\eta; v; w]$ respectively.

Therefore, in the above observer design process as Equation 3.15, the state estimate $\dot{\hat{x}}$ is formulated as:

$$\dot{\hat{x}}_{ob} = f(\boldsymbol{x}, \boldsymbol{\tau}, \boldsymbol{w}) + \boldsymbol{P} \boldsymbol{H}^{T} (\boldsymbol{H} \boldsymbol{P} \boldsymbol{H}^{T} + \boldsymbol{R})^{-1} (\boldsymbol{Y} - \boldsymbol{H} \hat{\boldsymbol{x}}), \tag{3.17}$$

where

$$\dot{\mathbf{P}} = \frac{\partial f}{\partial \hat{\mathbf{x}}_{ob}} \mathbf{P} + \mathbf{P} \frac{\partial f^{T}}{\partial \hat{\mathbf{x}}_{ob}} + \mathbf{G} \mathbf{Q} \mathbf{G}^{T} - \mathbf{P} \mathbf{H}^{T} (\mathbf{H} \mathbf{P} \mathbf{H}^{T} + \mathbf{R})^{-1} \mathbf{H} \mathbf{P}.$$
(3.18)

The stability of using the EKF for force estimation has been demonstrated in [29]). Accordingly, the stability analysis of the proposed EAOB method can be conducted using two theorems.

Theorem 1 The proposed EAOB for the system described in Equation 2.33 is locally

stable, given that

1.
$$\alpha_1 \mathbf{I} \le ||\mathbf{Q}(t)|| \le \alpha_2 \mathbf{I}$$
,

2.
$$\alpha_3 \mathbf{I} \leq ||\mathbf{R}_k|| \leq \alpha_4 \mathbf{I}$$
.

3. Then the following is true:

$$\alpha_5 \mathbf{I} \le \int_t^{t+\sigma} \mathbf{F_{23}}(\boldsymbol{\tau})^T \mathbf{F_{23}}(\boldsymbol{\tau}) d\boldsymbol{\tau} \le \alpha_6 \mathbf{I}$$
(3.19)

where $F_{23}(\tau)$ in Equation 3.12 is bounded based on Assumption 1, and α_{1-6} are positive constants.

Theorem 2 Assume that the model of a linearized system is

- 1. uniformly completely observable,
- 2. uniformly completely controllable,

3.
$$\alpha_1 \mathbf{I} < \|\mathbf{Q}(t)\| < \alpha_2 \mathbf{I}$$
,

4.
$$\alpha_3 \mathbf{I} \leq ||\mathbf{R}_k|| \leq \alpha_4 \mathbf{I}$$
,

5.
$$\|\mathbf{F}(t)\| \le \alpha_5, \|\mathbf{G}(t)\| \le \alpha_6, \|\mathbf{H}_k\| \le \alpha_7.$$

Then the following equation which derived from Equation 3.15 is true

$$\dot{\hat{x}}_{ob} = F\hat{x}_{ob} + PH^{T}(HPH^{T} + R)^{-1}H\tilde{x}_{ob},
\dot{\tilde{x}}_{ob} = [F - PH^{T}(HPH^{T} + R)^{-1}H]\tilde{x}_{ob},$$
(3.20)

is uniformly asymptotically stable based on [30], where $\tilde{\mathbf{x}} = \mathbf{x} - \hat{\mathbf{x}}$ is the unforced optimal filter.

As per Theorem 2, it is necessary to linearize the nonlinear dynamic system. The linearized system can be constructed with Equation 3.10 and 3.11 as follows:

$$\dot{x}_{ob} = F(t)x_{ob} + G\xi_x,
z = Hx_{ob} + V_k.$$
(3.21)

To ensure the stability of the EAOB, certain conditions must be met. Firstly, the linearized system must be fully observable, which can be achieved by satisfying conditions 2 and 3 in Theorem 1. Secondly, the linearized system must be fully controllable, which can be accomplished by meeting condition 1 in Theorem 1. Finally, stability can be achieved by utilizing the outcomes of Theorem 2.

3.2.3 MPC Implementation

MPC is a model based control strategy, which determines the control action by recursively solving OCPs and respects the system constraints during the control, as shown in Figure 3.1.

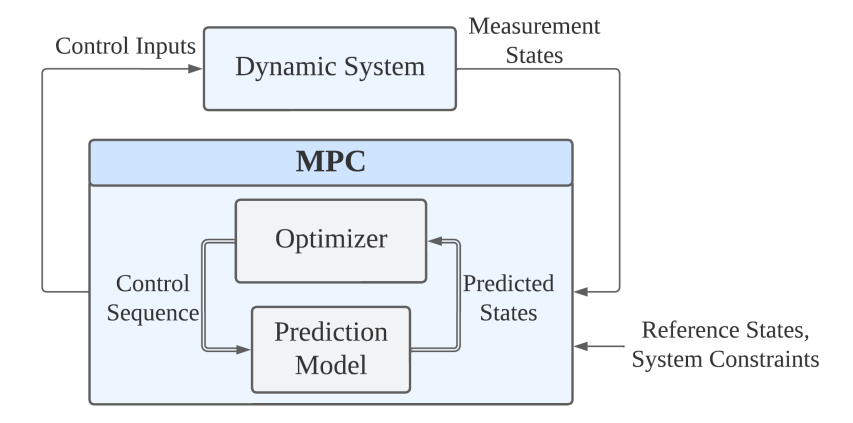


Figure 3.1: Control loop of the MPC, which mainly includes an optimizer and a prediction model.

In the MPC control loop, it receives reference states, system constraints and mea-

surement states from the dynamic system, and outputs the control inputs back to the system. The MPC calculates the predicted outputs based on the prediction model with a sequence of control inputs over a certain horizon, and the optimizer solves the Quadratic Programming (QP) problem as:

$$\min_{U,X} \int_{t=0}^{T} \|h(\boldsymbol{x}(t), \boldsymbol{u}(t)) - \boldsymbol{y_{ref}}\|_{\boldsymbol{Q_c}}^{2} dt + \|h(\boldsymbol{x}(T)) - \boldsymbol{y_{N,ref}}\|_{\boldsymbol{Q_N}}^{2}$$
subject to $\dot{\boldsymbol{x}} = f(\boldsymbol{x}(t), \boldsymbol{u}(t));$

$$\boldsymbol{u}(t) \in \mathbb{U}$$

$$\boldsymbol{x}(t) \in \mathbb{X}$$

$$\boldsymbol{x}(0) = x(t_0).$$
(3.22)

where u(t) and x(t) represent control inputs and system states at time t; T is the prediction horizon which refers to the number of time steps to look forward; y_{ref} and $y_{N,ref}$ are the stage reference states in the prediction horizon and the terminal reference states respectively; Q_c and Q_N are the weighting matrics for stage states and terminal states; $f(\cdot)$ and $h(\cdot)$ are the prediction model and system output function; and \mathbb{U} and \mathbb{X} are constraints in control inputs and system states.

When designing a real-world system, it is important to consider the input constraints based on the physical limits of the actuator being used. In this case, the control inputs u are bounded, as $|u_1| \leq f_{max}$, $|u_2| \leq f_{max}$, $|u_3| \leq f_{max}$, $|u_4| \leq M_{max}$. f_{max} and M_{max} represent the maximum allowed force and moment limits, respectively. The f_{max} and M_{max} are determined based on the propeller thrust force datasheet in [22]. In this study, the MPC also takes system constraints into account. The vehicle's linear velocity are limited as $|u| \leq v_{max}$, $|v| \leq v_{max}$, and $|w| \leq v_{max}$. Here, v_{max} represents the maximum linear velocity. The v_{max} is determined based on the system's specification in [10], while $v_{max} = 1.5m/s$. To ensure that the constraints are taken into account during optimization and further assure control feasibility, the input constraints are written into \mathbb{U} , while the

system constraints are written into X in the cost function in Equation 3.22.

To tune the MPC, there are several important steps to follow. First, the prediction horizon T is selected, taking into account the trade-off between control performance and computational burden. To find an optimal value that balances these factors, the horizon is incrementally increased during simulations and evaluated for improved control performance while maintaining real-time operation of the MPC. Additionally, MPC allows for the prioritization of multiple control objectives by assigning weighting factors in the matrix Q_c to each objective. In this particular work, the yaw angle ψ is given the highest priority, followed by the position states x, y, and z. The terminal cost is associated with the final state of the system at the end of the prediction horizon. The weighting matrix at terminal states Q_N reflects the relative significance of achieving the desired steady-state or target. A higher weight indicates a stronger emphasis on reaching the desired terminal state. However, since the focus of this work is on the robustness of the controller, Q_N is set equal to the values in Q_c to provide less aggressive control.

Once the MPC has been fine-tuned to attain the desired control performance, the proposed EAOB, as described in Section 3.2, can be incorporated into the MPC. The estimated states $\hat{x}_{k|k}$ provided by the EAOB are divided into two components. The first component consists of the estimated positions $\hat{\eta}$ and velocities \hat{v} , which are utilized by the MPC module to enhance the accuracy of the system states. Simultaneously, the second component, the estimated disturbances \hat{w} , is incorporated into the MPC's prediction model as Equation 2.33 at each time step. According to Assumption 2, the disturbance term throughout the prediction horizon T remains consistent with the estimated disturbance \hat{w} at the current time step.

Therefore, the DOBMPC algorithm is implemented in a receding horizon as following steps:

1. At the sampling time instant, utilize prediction equation 3.14 and update equation 3.15 to estimate the disturbance $\hat{\boldsymbol{w}}$ using the EAOB approach.

- 2. Update the parameters within the disturbance term \boldsymbol{w} in the prediction model of the MPC, as represented by Equation 2.33, at the current time instant and within the prediction horizon [0,T], by incorporating the estimated disturbance $\hat{\boldsymbol{w}}$ obtained in the initial step.
- 3. The OCP in the Equation 3.22 is solved to obtain the optimized control sequence $\boldsymbol{u}^*(s), s \in [0, T].$
- 4. The first set of the control sequence $u^*(s)$, $s \in [0, \Delta t]$ is implemented in the dynamic system, while the rest will be treated as initial condition in the next iteration.
- 5. At the next sampling instant, the OCP in the Equation 3.22 will be solved again with the measurement states and new initial condition.

By integrating the EAOB with MPC, the parameters within the disturbance term \boldsymbol{w} in the MPC's prediction model are continuously updated at each time step, as outlined in step 2. This integration results in a nonlinear parameter-varying model. Consequently, the MPC's optimizer incorporates the estimated disturbances, enabling it to generate optimal control inputs that effectively reject disturbances at each iteration.

To realize the MPC, the OCP should be discretized from t_0 to t_T and solved with multiple shooting schemes. Therefore, it becomes a Sequential Quadratic Program (SQP) which is executed in a real-time iteration scheme [31]. In this research work, the implementations are completed through ACADOS [32]. ACADOS is a versatile and efficient open-source optimization framework designed specifically for real-time MPC applications. It follows a two-stage approach, consisting of an offline stage and an online stage. In the offline stage, ACADOS defines the system dynamics, cost function, and constraints, formulating the MPC problem as a Nonlinear Programming (NLP). It compiles this representation into a solver-ready format. In the online stage, ACADOS solves the NLP in real-time, taking the current system state as input and iteratively optimizing the control inputs while satisfying the dynamics and constraints. ACADOS offers various advantageous functionalities,

such as efficient numerical algorithms, real-time capabilities, and the flexibility to choose solvers, constraints, and objective functions based on specific requirements.

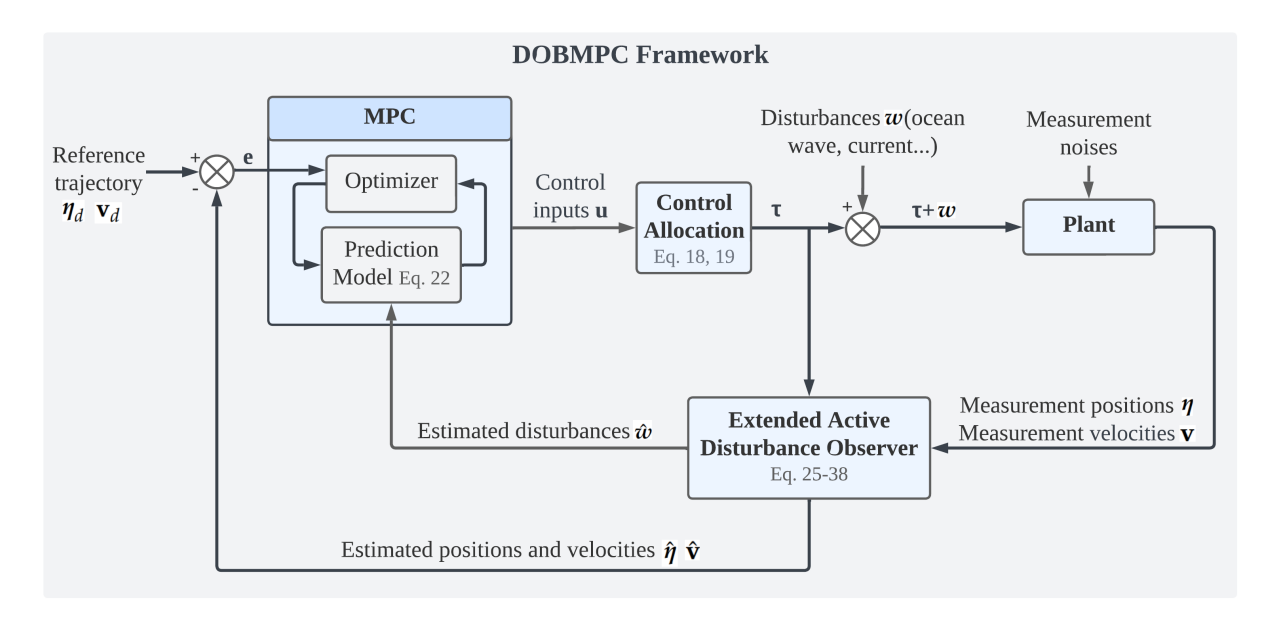


Figure 3.2: Block diagram of the proposed DOBMPC scheme with disturbance compensation incorporated.

The overall block diagram of the proposed DOBMPC is depicted in Figure 3.2. The EAOB module receives measurements of positions η , velocities v, and propulsion forces and moments τ . It then outputs the estimated positions $\hat{\eta}$, velocities \hat{v} , and disturbances \hat{w} . The MPC module utilizes the estimated positions $\hat{\eta}$ and velocities \hat{v} as system states. It generates control inputs u based on the error e between the reference trajectory (comprising positions η_d and velocities v_d) and the system states. The estimated disturbances \hat{w} are directly written into the MPC prediction model, as illustrated in the figure. The resulting optimal control inputs u, which account for the disturbances, are then passed through the control allocation process to drive the system plant.

3.3 Results

The performance of the proposed DOBMPC is validated through simulation using the UUV Simulator [33], an extension of the open-source robotics simulator Gazebo tailored for underwater scenarios, enhancing realism in the simulation environment.

In practical applications, obtaining measurements of system states, including linear and angular position along with linear and angular velocity, is essential. In underwater settings where GPS signals are unavailable, alternative sensors come into play. Underwater acoustic positioning systems like Ultra-Short Baseline (USBL) are favored for their mobility, offering reliable linear position data for the UUV. The AHRS aids in determining the UUV's angular position (pitch, roll, and yaw) for acquiring crucial attitude details. Gyroscopes within the AHRS facilitate angular velocity estimation. Determining linear velocity often involves using a DVL for UUVs. However, a cost-effective alternative method estimates velocity based on thrust and a fixed thrust-velocity relationship at steady state, albeit potentially with reduced accuracy, especially in the presence of significant external disturbances.

The BlueROV2's specifications in this study are outlined in a Unified Robot Description Format (URDF) file, representing the robot model. This model in the URDF file aligns with the dynamic model in Section 2.2, detailing parameters such as mass m, weight W, buoyancy B, and inertia I_x , I_y , and I_z in Table 3.1 for the rigid body parameters. Table 3.2 specifies hydrodynamic terms, including added mass due to UUV movement through fluid and linear damping from skin friction.

In the tests for rejecting disturbances, two tasks in motion control are addressed, namely dynamic positioning and following desired paths. The performance of the proposed DOBMPC is assessed against conventional PID and standard MPC controllers. Following Fossen's principles [11], the disturbance component is characterized in terms of forces according to Equation 2.33. To evaluate how well disturbances are countered, disturbances

Table 3.1: BlueROV2 rigid-body parameters defined in URDF file.

Parameter	Value
\overline{m}	$11.26 \ kg$
W	$112.8 \ N$
B	$114.8 \ N$
I_x	$0.3~kgm^2$
I_y	$0.63~kgm^2$
I_z	$0.58~kgm^2$

Table 3.2: BlueROV2 hydrodynamic parameters defined in URDF file.

Direction	Parameter	Value
Surge	$X_{\dot{u}}$	$1.7182 \ kg$
Sway	$Y_{\dot{v}}$	$0 \ kg$
Heave	$Z_{\dot w}$	5.468~kg
Roll	$K_{\dot{p}}$	$0 \ kgm^2/rad$
Pitch	$M_{\dot{q}}$	$1.2481 \ kgm^2/rad$
Yaw	$N_{\dot{r}}$	$0.4006 \ kgm^2/rad$
Surge	X_u	$-11.7391 \ Ns/m$
Sway	Y_v	$-20 \ Ns/m$
Heave	Z_w	$-31.8678 \ Ns/m$
Roll	K_p	-25 Ns/rad
Pitch	M_q	$-44.9085 \ Ns/rad$
Yaw	N_r	-5 Ns/rad

are simulated as body wrenches, encompassing forces and moments across 4 degrees of freedom. By utilizing the ROS service ApplyBodyWrench, forces and moments acting at the CG of the UUV in the IRF are generated. Consequently, to compare outcomes, the rotation matrix outlined in Equation 2.9 is necessary to transform the disturbances \boldsymbol{w} estimated in the BRF to the IRF.

Table 3.3 provides a breakdown of the parameters for the MPC, which are applicable to both the proposed DOBMPC and the standard MPC used as a reference. The baseline MPC employed for comparison adopts the identical cost function as the proposed DOBMPC outlined in Equation 3.22. With a prediction horizon of 60 and a sampling

time of 0.05 seconds, the system looks ahead by 3 seconds. The average computational time for solving the OCP tasks stands at 7 milliseconds, ensuring real-time operation. The PID parameters employed in this study are also detailed in Table 3.4. The implemented PID controller leverages the system's positional states η and velocity v, along with the control inputs encompassing forces and moments τ . The control signals determined by the PID controller are subsequently distributed to each propeller through the control allocation methodology delineated in Equation 2.28.

Table 3.3: MPC parameters utilized in this work.

Controller parameters	Value
Prediction horizon	60
Sample time (s)	0.05
Q_c	[300 300 150 10 10 150 10 10 10 10 10 10 15 15 15 0.5]
Q_N	[300 300 150 10 10 150 10 10 10 10 10 10]
OCP time (ms)	7

Table 3.4: PID parameters utilized in this work.

Control gain	Surge	Sway	Heave	Yaw
K_p	5	5	5	7
K_i	0.05	0.05	0.05	0.1
K_d	1.2	1.2	1.2	0.6

3.3.1 Dynamic Positioning Results

In the context of dynamic positioning, the UUV faces two distinct forms of disturbances: periodic wave influences and persistent current effects. These disturbances materialize as forces and moments exerted on the UUV. Concerning periodic disruptions, sinusoidal waves with variable force magnitudes spanning from 10 to 16 N are exerted in the x_i , y_i , and z_i orientations, alongside sinusoidal waves with random moment magnitudes ranging from 1 to 2 Nm applied along the z_i axis.

The UUV is configured to maintain a fixed position at coordinates [0, 0, -20] within the IRF, with a yaw angle of 0 degrees, amidst external disruptions. Illustrated in Figure 3.3 are the inferred disturbances juxtaposed with the actual disturbances. The visualization demonstrates a close alignment between the estimated and actual disturbances, with the estimation lag falling below the sampling interval, affirming the viability of the proposed EAOB.

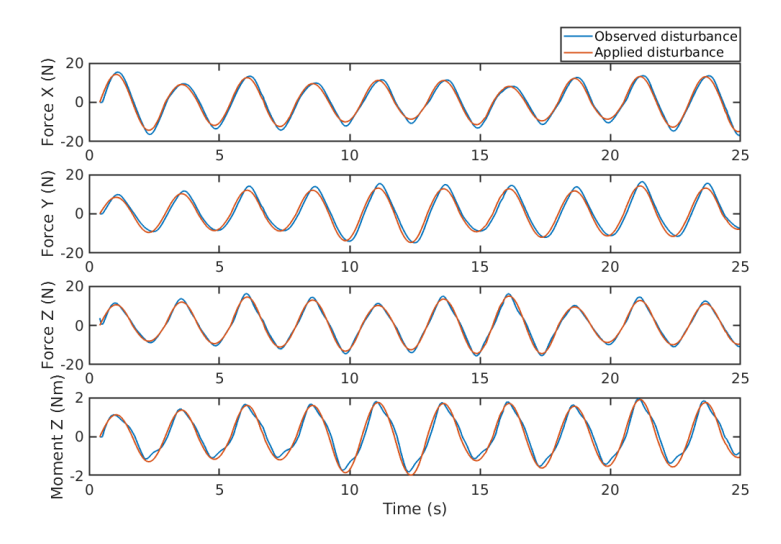


Figure 3.3: Disturbances estimation of periodic waves with random force and moment amplitudes.

By integrating the estimated disturbances into the predictive model of the MPC, the controller's ability to reject disturbances is significantly improved. This enhanced performance surpasses both the PID and the standard MPC approaches. The results are illustrated in Figure 3.4. Additionally, a two-dimensional representation showcasing the dynamic positioning outcomes of the three controllers is depicted in Figure 3.5, with the trajectory in blue highlighting the improved stability of the DOBMPC in maintaining the reference position.

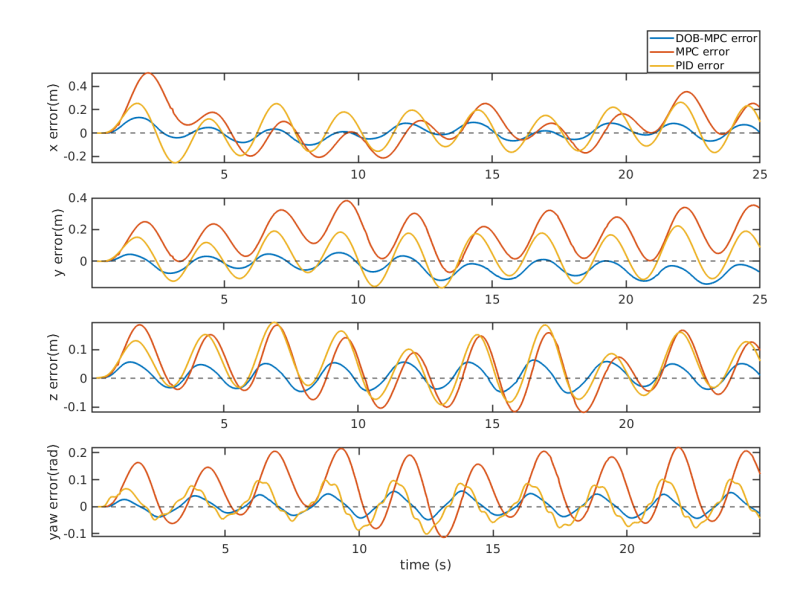


Figure 3.4: Tracking errors of the proposed DOBMPC, baseline MPC and PID controllers under periodic disturbances.

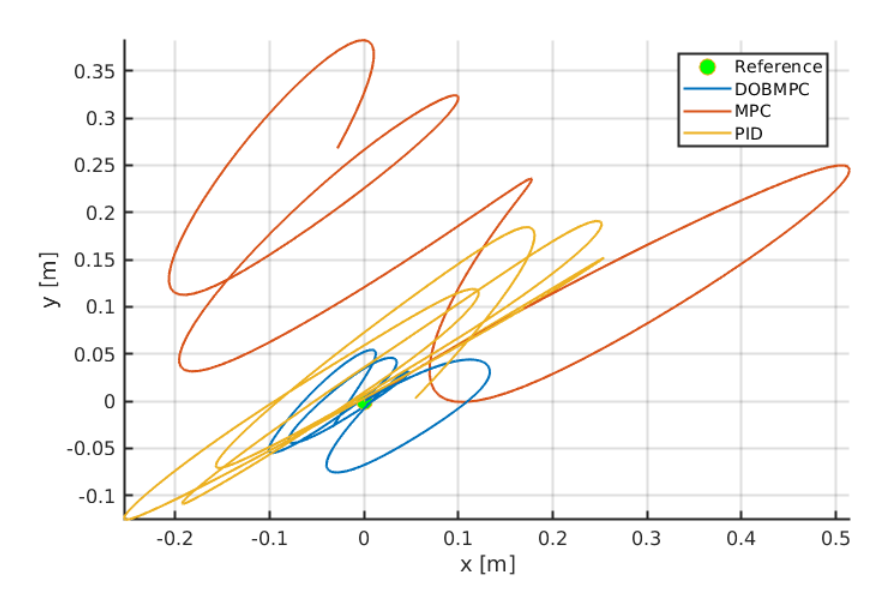


Figure 3.5: Trajectories of dynamic positioning results of the proposed DOBMPC, baseline MPC and PID controllers under periodic disturbances.

Figure 3.6 presents the control inputs associated with the proposed DOBMPC when subjected to periodic wave disturbances.

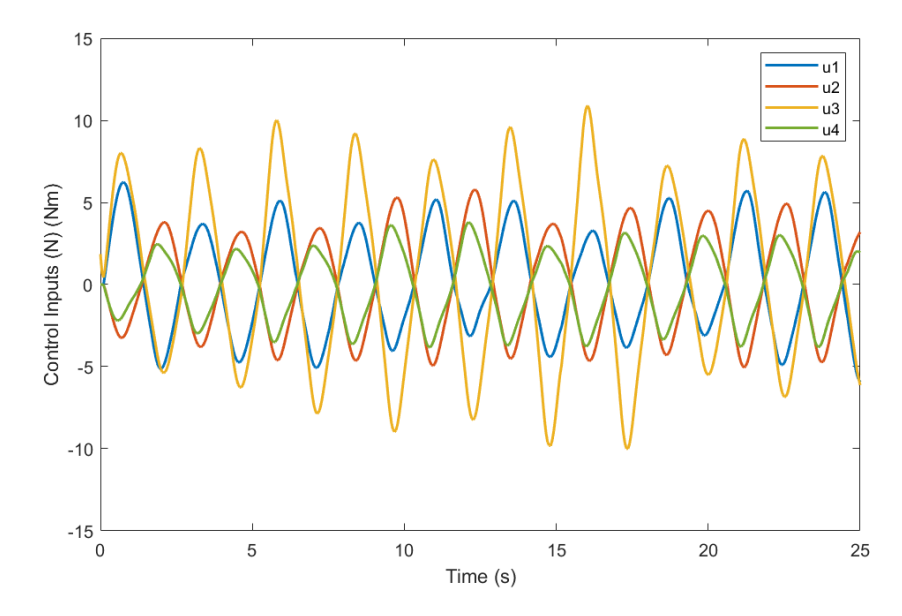


Figure 3.6: Control inputs of the proposed DOBMPC in surge, sway, heave and yaw direction for dynamic positioning under periodic wave effect.

To induce continual disturbances, a force of $10\ N$ is exerted along the $x_i,\,y_i,\,$ and z_i axes at time $t=10s,\,$ accompanied by a torque of $5\ Nm$ applied around the z_i axis simultaneously. In Figure 3.7, a minor overshoot is noticeable when the disturbances shift abruptly from $0\ N$ to $10\ N$. This overshoot arises due to substantial variations in estimated states between consecutive time steps. The EAOB mechanism corrects the estimated states with high accuracy within less than 0.5 seconds through iterative adjustments. Figure 3.8 illustrates the error tracking of the proposed DOBMPC, standard MPC, and PID controllers under constant currents, showcasing distinct levels of disturbance rejection ability. The DOBMPC controller adeptly estimates disturbances and compensates for them, leading to error convergence towards zero along each axis. The 2D plot in Figure 3.9 further elucidates the dynamic positioning performance of these controllers, revealing a marked enhancement in disturbance rejection capability with the implementation of the proposed DOBMPC.

The corresponding control inputs of the proposed DOBMPC for dynamic positioning

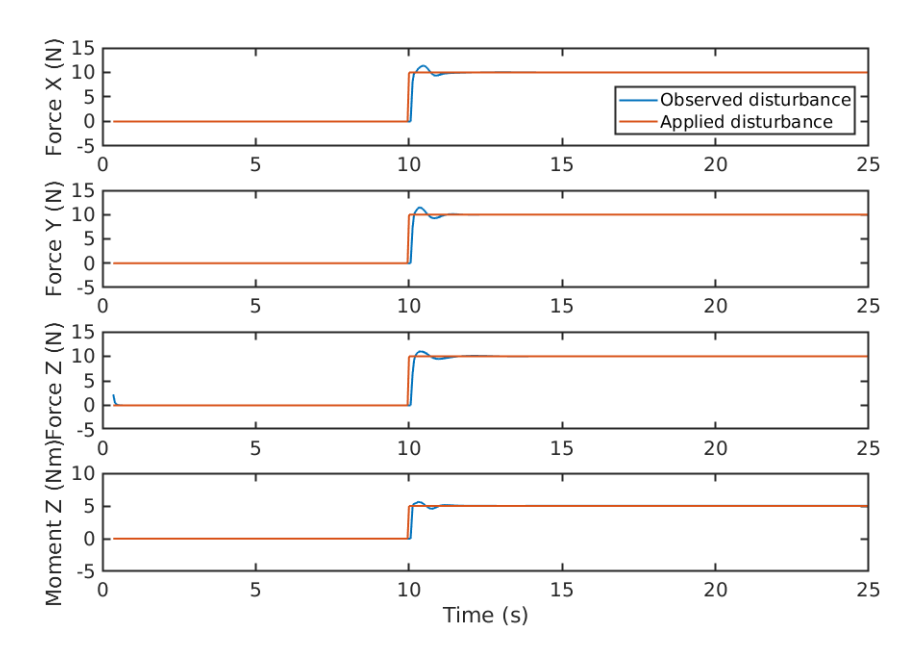


Figure 3.7: Disturbances estimation of constant currents in x, y, z directions.

under constant current effect is illustrated in Figure 3.10.

Furthermore, this study delves into evaluating the ability to reject disturbances when combining periodic wave and constant current influences in dynamic positioning scenarios. Sinusoidal waves with varying force amplitudes spanning from 3 to 6 N are administered in the x_i , y_i , and z_i directions, alongside sinusoidal waves with random moment amplitudes ranging from 1 to 2 Nm around the z_i axis. At time t = 4s, the constant current impact is superimposed with forces of 10 N in the x_i , y_i , and z_i directions, along with a torque of 3 Nm around the z_i axis. Figure 3.11 illustrates the comparison between the applied and estimated disturbances, showcasing a high degree of alignment. The error in tracking and the control inputs are depicted in Figure 3.12 and Figure 3.13, respectively.

3.3.2 Trajectory Tracking Results

To evaluate trajectory tracking performance, two distinct movement scenarios are utilized. Initially, a circular trajectory with a radius of 2 meters is employed, with the yaw angle of

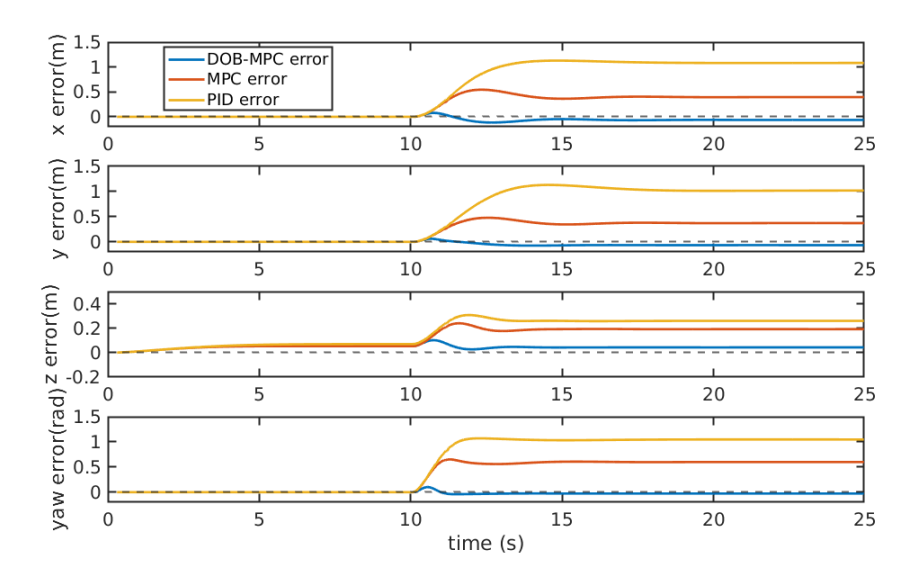


Figure 3.8: Tracking errors of the proposed DOBMPC, baseline MPC, and PID controllers under constant currents.

the UUV defined relative to the surge direction. To gauge the system's resilience, a 10 N force is exerted in the x_i , y_i , and z_i directions, accompanied by a 5 Nm torque around the z_i axis. Figure 3.14 presents a comparison between the estimated disturbances and the actual disturbances. The periodic disturbances in the X and Y directions during a UUV's circular trajectory can be classified as unmodeled dynamics because the observer's nominal model may not fully capture the nonlinear hydrodynamic effects, such as added mass and Coriolis forces, which vary periodically with the vehicle's motion. These unmodeled effects are misinterpreted as external disturbances, leading to the observed periodic fluctuations. The observed differences between the estimated and actual disturbances can be attributed to unmodeled components within the disturbance term originating from the nonlinear damping forces encountered by the UUV during circular trajectory motion.

The tracking errors of the PID, standard MPC, and the proposed DOBMPC are displayed in Figure 3.15, showcasing a notable decrease in tracking errors with the implementation of the proposed DOBMPC. Furthermore, Figures 3.16 and 3.17 offer a visual representation of the trajectory tracking outcomes. The control inputs corresponding to the proposed DOBMPC are depicted in Figure 3.18.

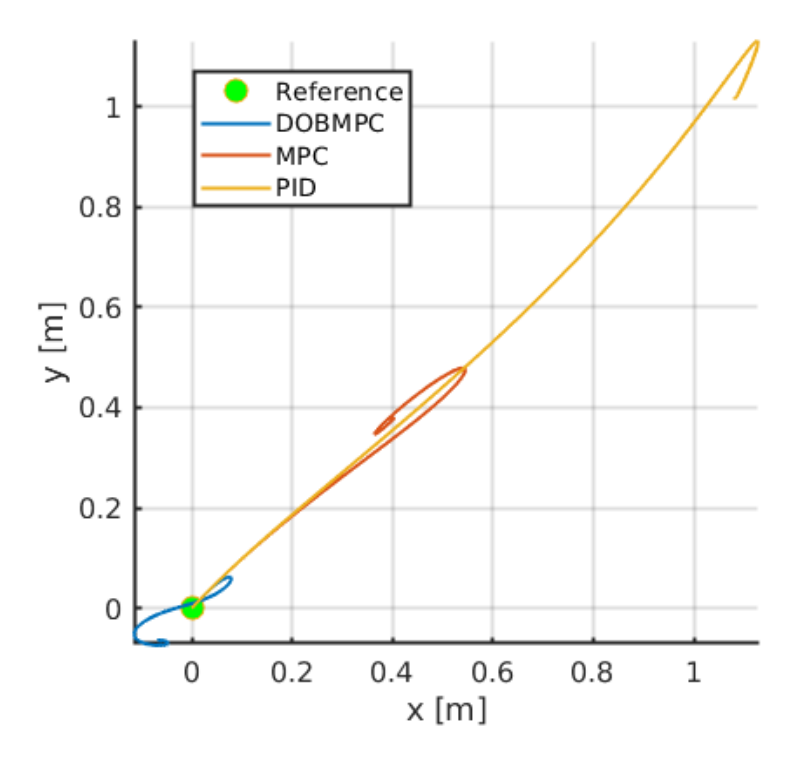


Figure 3.9: Trajectories of dynamic positioning results of the proposed DOBMPC, baseline MPC, and PID controllers under constant currents.

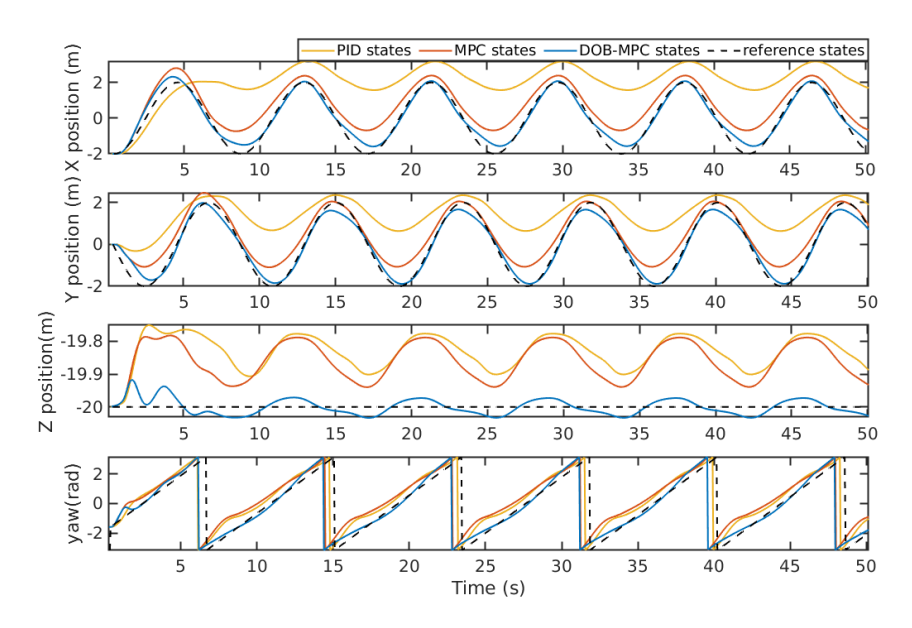


Figure 3.16: Circular trajectory tracking results of the proposed DOBMPC, baseline MPC, and PID controllers in x, y, z, and yaw directions.

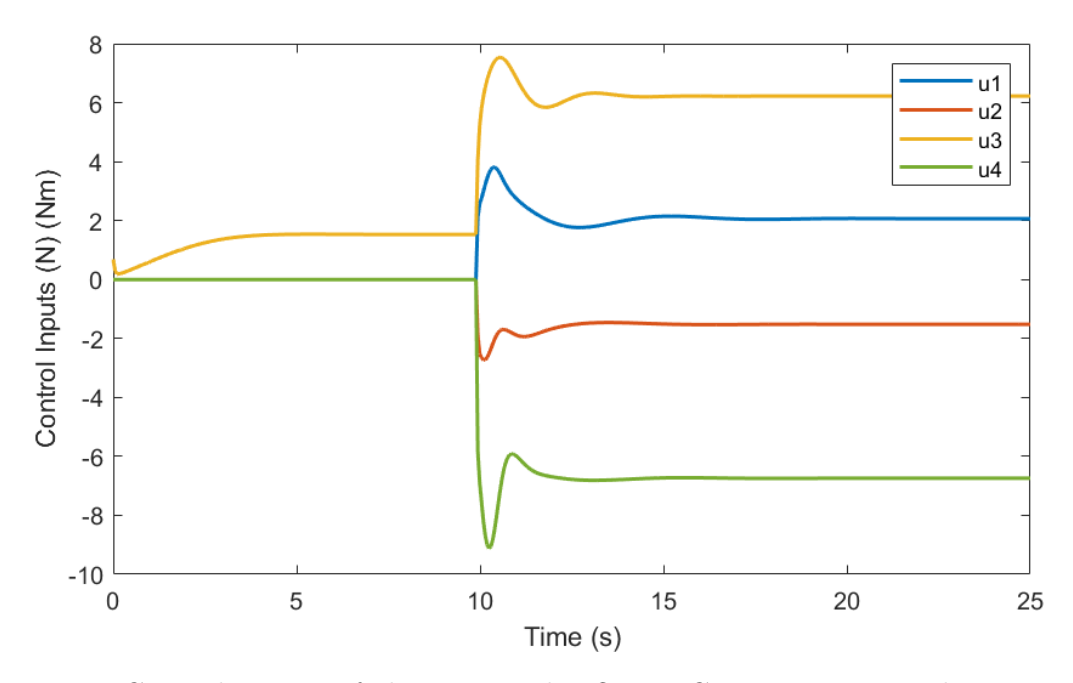


Figure 3.10: Control inputs of the proposed DOBMPC in surge, sway, heave and yaw direction for dynamic positioning under constant currents.

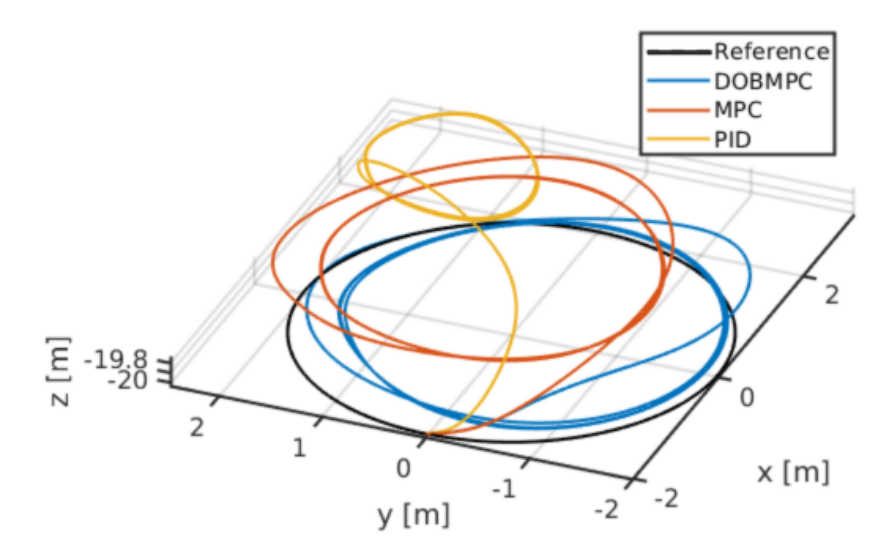


Figure 3.17: Three-dimensional circular trajectory tracking results of the proposed DOBMPC, baseline MPC, and PID controllers.

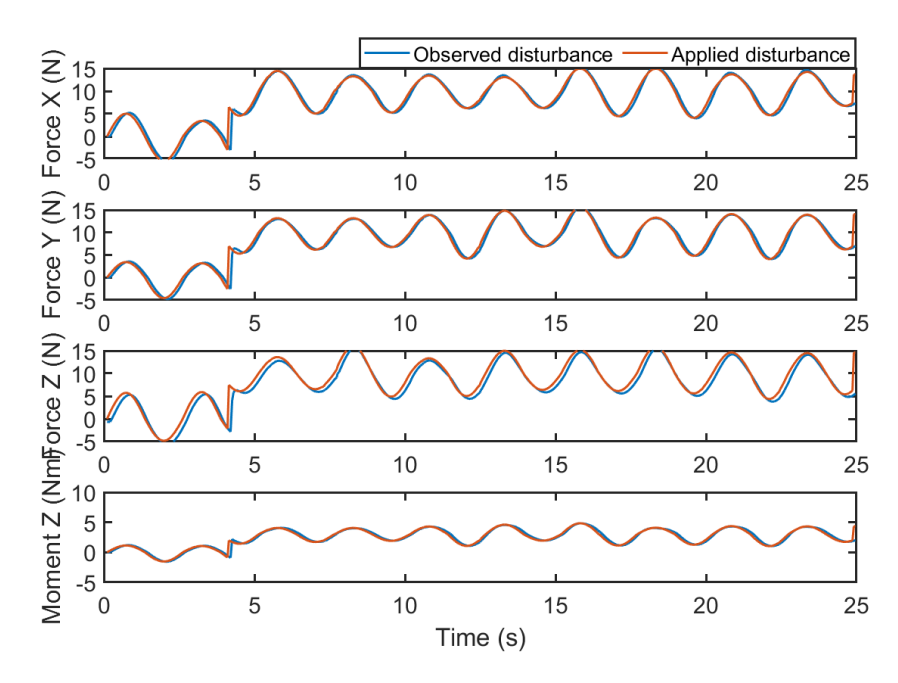


Figure 3.11: Disturbances estimation of superposition of periodic wave and constant current effect in x, y, z directions.

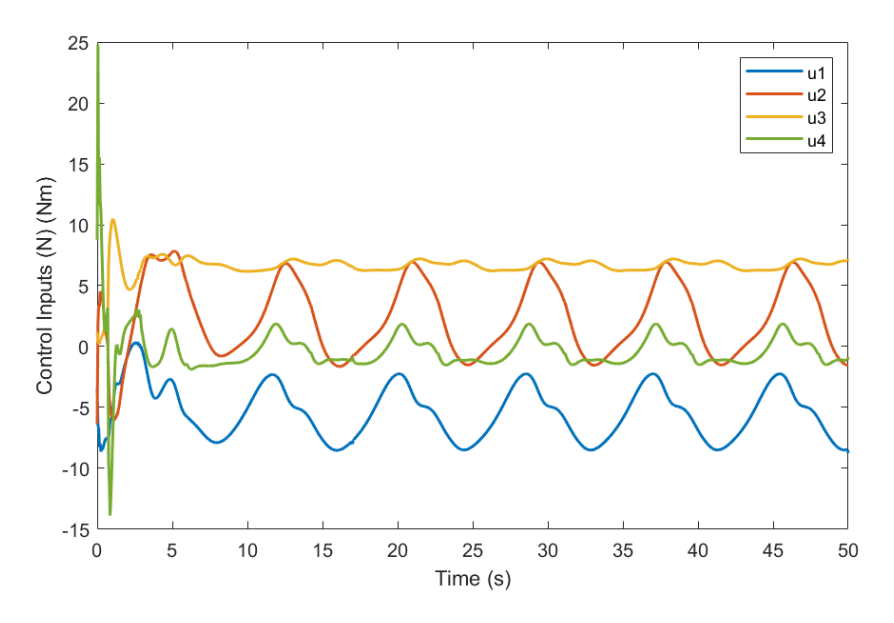


Figure 3.18: Control inputs of the proposed DOBMPC in surge, sway, heave, and yaw direction for tracking circular trajectory under constant currents.

To assess the efficacy of the proposed control methodology in tracking a highly intricate nonlinear path, a lemniscate trajectory with a 2-meter amplitude is employed. The yaw angle remains constant at 0 degrees throughout the motion, with periodic wave

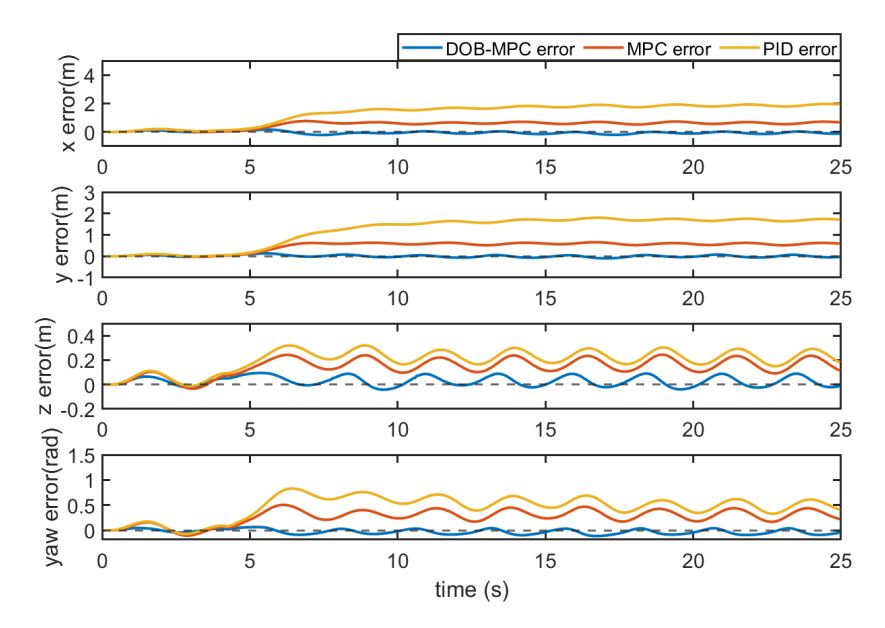


Figure 3.12: Tracking errors of the proposed DOBMPC, baseline MPC, and PID controllers under superposition of periodic wave and constant current effect.

effects integrated into the evaluation phase. These waves encompass random force amplitudes ranging from 10 to 16 N and random moment amplitudes ranging from 2 to 4 Nm. Figure 3.19 presents a comparison between the generated disturbances and the estimated disturbances. The outcomes reveal that the disturbance forces in the x_i , y_i , and z_i directions can be accurately estimated when following a lemniscate trajectory. However, challenges arise in accurately estimating the disturbance moment around z_i during the tracking of this trajectory, leading to occasional deviations or noise around the actual disturbance value. The intricate nature of unmodeled nonlinear hydrodynamics, particularly pronounced when tracking a nonlinear trajectory like the lemniscate, may contribute to this issue.

In Figure 3.20, the system states during the tracking of a lemniscate trajectory under periodic waves are compared across the PID, MPC, and the proposed DOBMPC. While the states of the PID and MPC exhibit irregularities due to time-varying significant disturbances, the states of the DOBMPC remain notably smoother. The tracking error, as depicted in Figure 3.21, shows a marked reduction with the proposed DOBMPC in contrast to the PID and MPC methods. Lastly, Figure 3.22 offers a three-dimensional visual

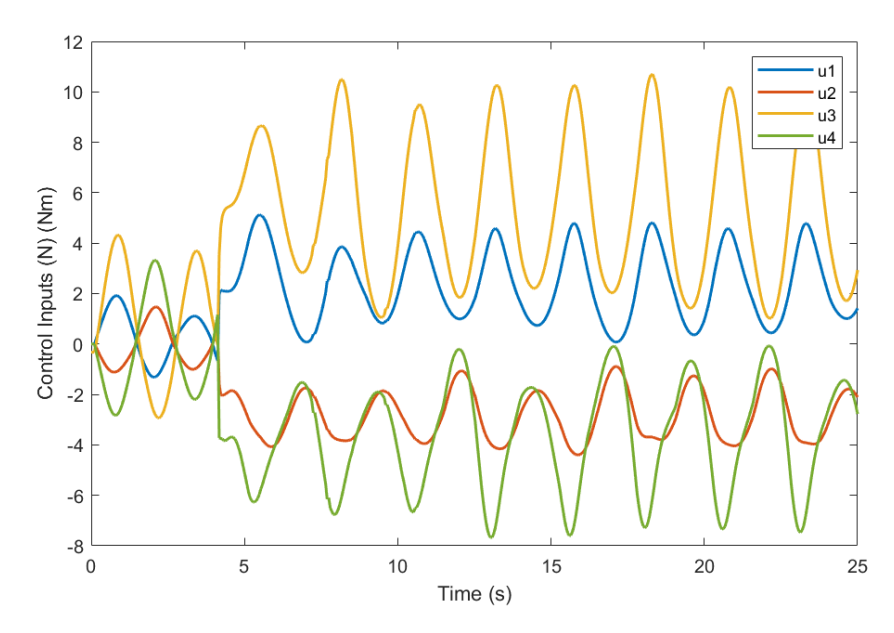


Figure 3.13: Control inputs of the proposed DOBMPC in surge, sway, heave and yaw direction for dynamic positioning under superposition of periodic wave and constant current effect.

representation of the trajectory tracking outcomes. The control inputs corresponding to the proposed DOBMPC for tracking the lemniscate trajectory are illustrated in Figure 3.23.

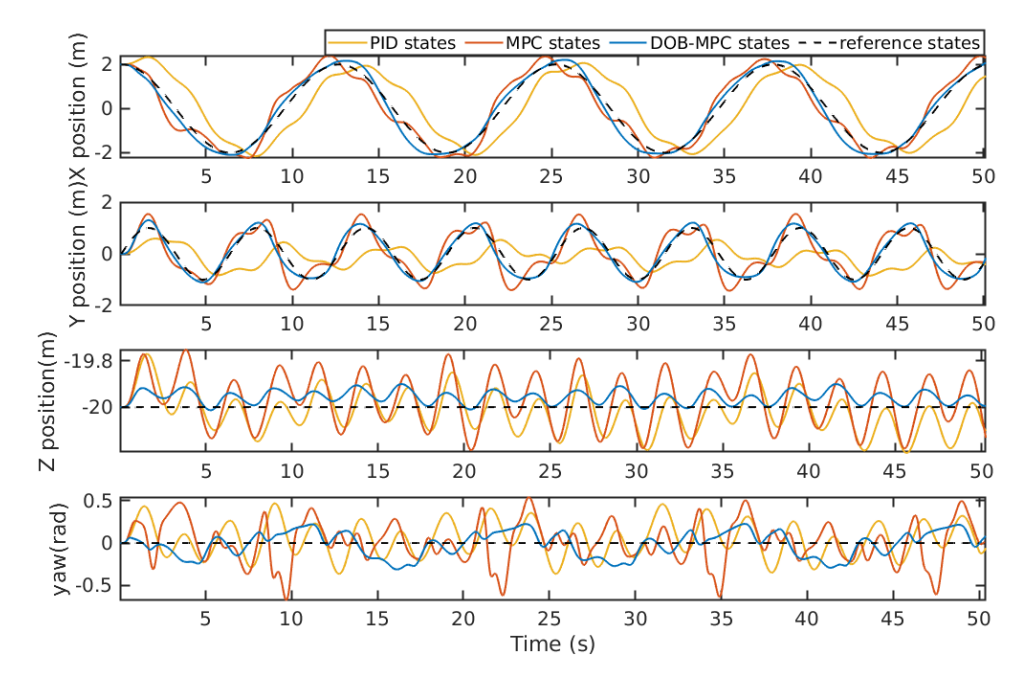


Figure 3.20: Lemniscate trajectory tracking results of the proposed DOBMPC, baseline MPC, and PID controllers in x, y, z, and yaw directions.

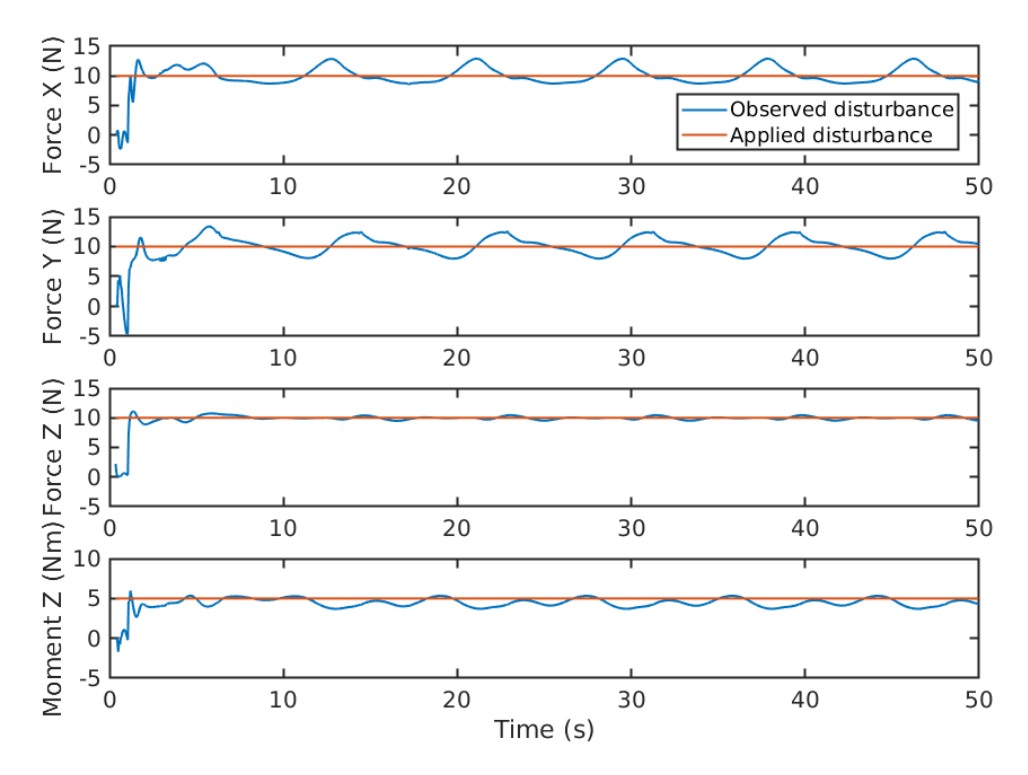


Figure 3.14: Disturbances estimation of constant currents during circular trajectory tracking.

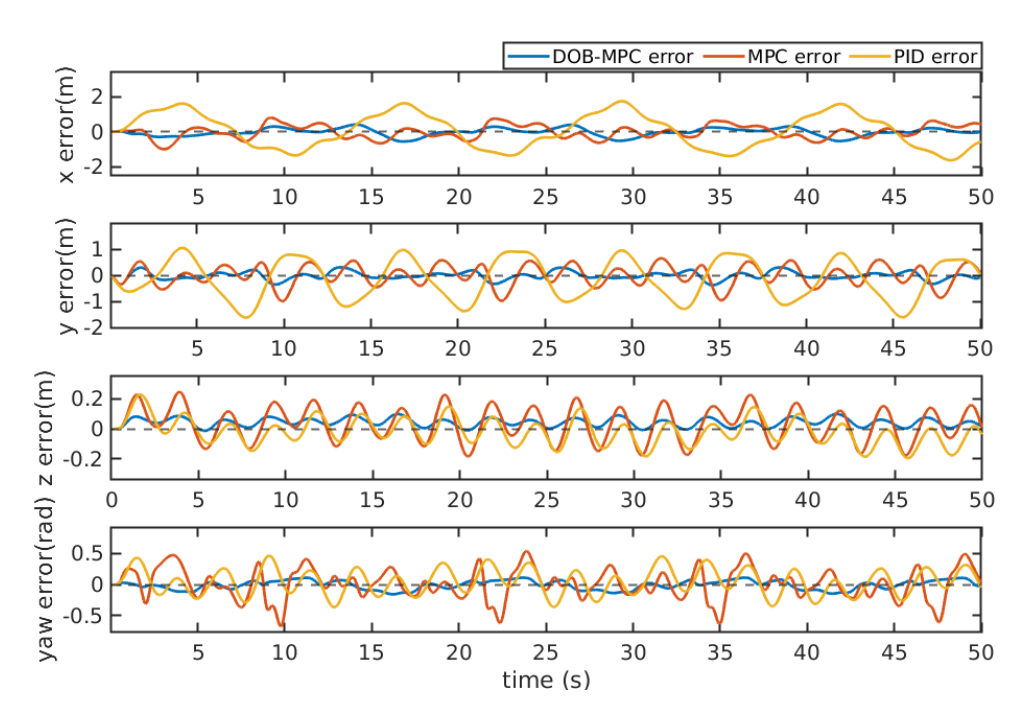


Figure 3.21: Tracking errors of the proposed DOBMPC, baseline MPC, and PID controllers under constant currents during lemniscate trajectory tracking.

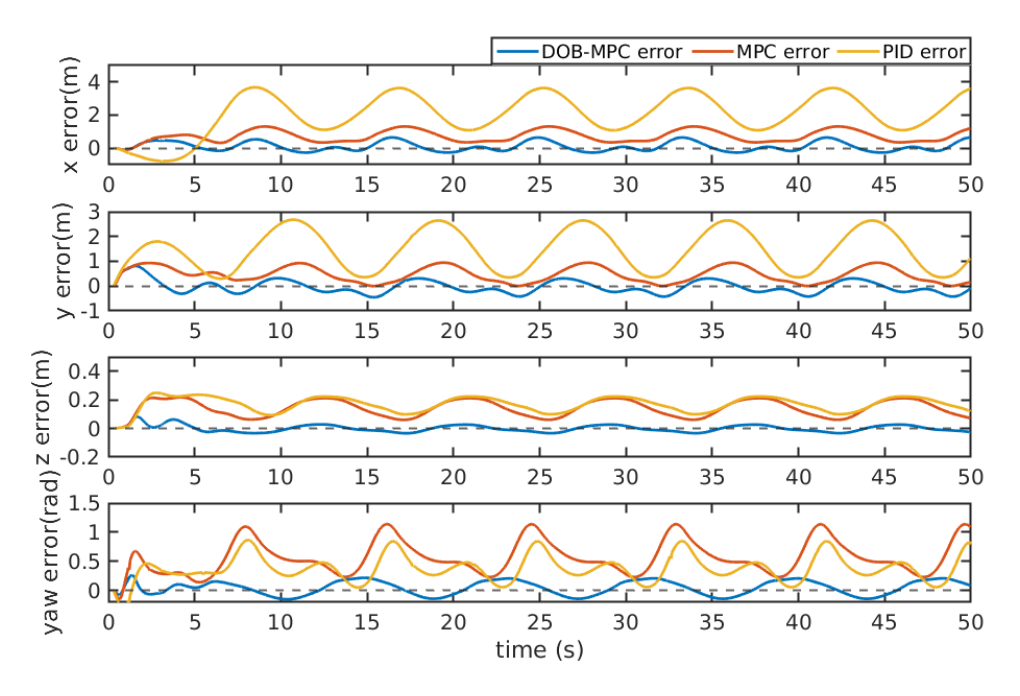


Figure 3.15: Tracking errors of the proposed DOBMPC, baseline MPC, and PID controllers under constant currents during circular trajectory tracking.

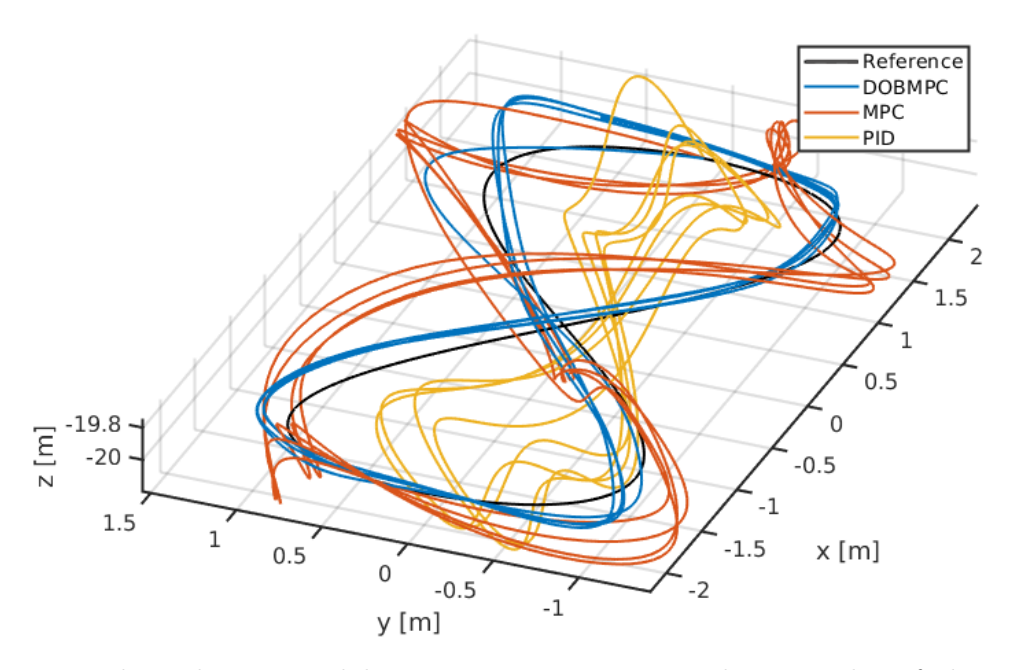


Figure 3.22: Three-dimensional lemniscate trajectory tracking results of the proposed DOBMPC, baseline MPC, and PID controllers.

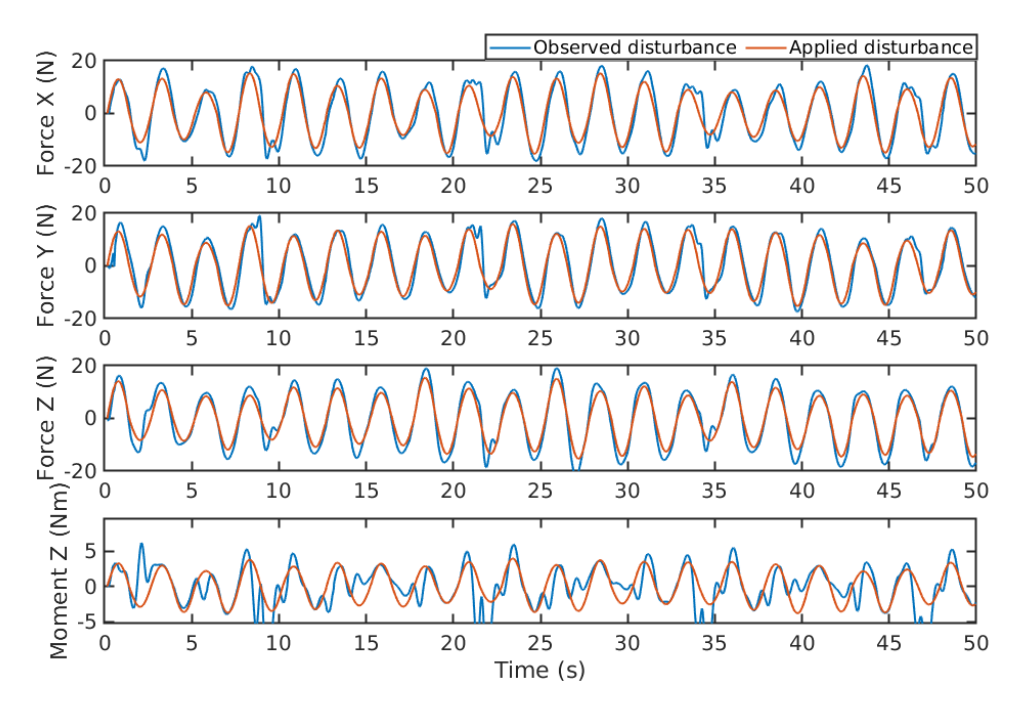


Figure 3.19: Disturbances estimation of periodic waves during lemniscate trajectory tracking.

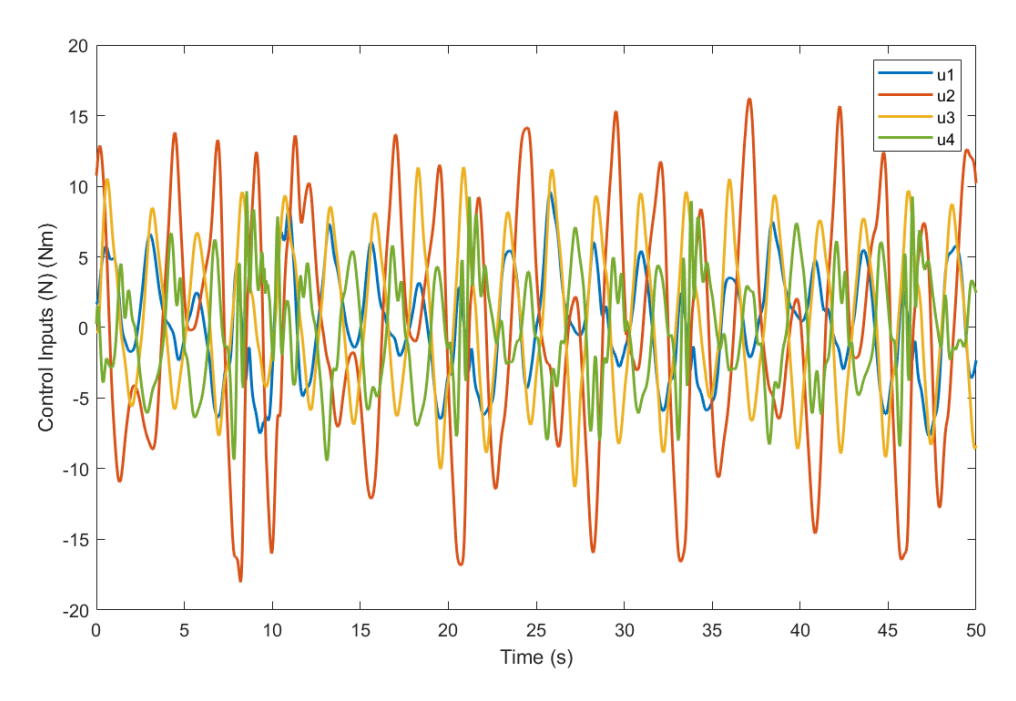


Figure 3.23: Control inputs of the proposed DOBMPC in surge, sway, heave, and yaw direction for tracking lemniscate trajectory under periodic waves.

3.3.3 Results Analysis

The figures above illustrate that the proposed observer can effectively estimate disturbances arising from both periodic wave effects and constant current effects, showcasing an aptitude for capturing unmodeled dynamics. Nonetheless, it is evident that at high frequencies of periodic wave effects, the observer's accuracy in estimating disturbances may diminish. This limitation arises due to the assumption that the disturbance term represents a slowly time-varying signal.

In Table 3.5, an assessment of the dynamic positioning and trajectory tracking performance of the UUV is presented based on the Root Mean Square Error (RMSE). The RMSE metric is commonly employed in control systems literature as a performance measure and is widely recognized for its utility in comparing and interpreting results across various controllers. By offering a quantitative measure, RMSE facilitates the evaluation and ranking of different control strategies. Moreover, RMSE is less influenced by outliers compared to metrics like Mean Absolute Error (MAE). By considering squared errors, RMSE accentuates the impact of larger errors, making it suitable for assessing the performance of control systems where extreme errors may occur.

The minimum RMSE value in each row is emphasized in the table. The outcomes distinctly indicate that the incorporation of the proposed DOBMPC substantially bolsters the system's capacity to mitigate disturbances.

3.4 Conclusion

In this chapter, a reliable DOBMPC has been designed for the dynamic positioning and trajectory tracking tasks of an UUV in the face of unexpected disturbances. The results from simulations demonstrate the effectiveness of the proposed control method in rejecting

Table 3.5: RMSE of the proposed DOBMPC, baseline MPC, and PID controllers in dynamic positioning and trajectory tracking.

Motion	Disturbance	Direction	PID (m)	MPC (m)	DOBMPC (m)
		X	0.1374	0.1689	0.0537
Dynamic	Periodic	Y	0.1095	0.1934	0.0605
Positioning	wave effects	\mathbf{Z}	0.0871	0.0896	0.0350
		Yaw	0.0536	0.1108	0.0282
		X	0.7893	0.3099	0.0521
Dynamic	Constant	Y	0.7544	0.2882	0.0482
Positioning	current effects	Z	0.2032	0.1508	0.0469
		Yaw	0.7858	0.4547	0.0491
	Superposition	X	1.4991	0.5666	0.0932
Dynamic	of wave	Y	1.3921	0.5151	0.0501
Positioning	and currents	Z	0.2179	0.1603	0.0486
		Yaw	0.5141	0.3039	0.1100
Circular		X	2.3626	0.8012	0.2924
Trajectory	Constant	Y	1.6433	0.5521	0.2629
Tracking	current effects	\mathbf{Z}	0.1763	0.1510	0.0233
		Yaw	0.4355	0.6325	0.2582
Lemniscate		X	0.9854	0.3764	0.2306
Trajectory	Constant	Y	0.7732	0.3844	0.1504
Tracking	current effects	\mathbf{Z}	0.0877	0.1133	0.0510
		Yaw	0.2059	0.2413	0.1457

disturbances. The proposed control method brings several key advantages. It firstly shows the capability to instantly estimate varying disturbances, ensuring swift compensation. Secondly, it proves tolerance to measurement noises by incorporating EKF algorithm, guaranteeing consistent performance. Furthermore, the MPC structure ensures that system constraints are accounted for when solving the OCP iteratively, thus keeping the UUV system within set boundaries. The estimated disturbances are directly integrated into the MPC's predictive model at each step, facilitating the computation of an optimal control strategy.

However, in this section, the hydrodynamic damping forces D(v) were considered into the MPC prediction model using ground truth data from Gazebo. As a result, in the preceding results, these forces were not classified as part of the disturbance term w.

However, in practical scenarios, measuring damping coefficients directly is challenging, and they can exert significant and rapidly changing forces on the UUV due to their positive correlation with velocities. Including the entire damping forces as a superposition in the disturbance term could potentially impact the optimization process negatively. Therefore, the online system identification algorithm is considered in this control framework in the following chapter to address this challenge.

Chapter 4

Model Predictive Control with Online System Identification

This chapter expands upon Chapter 3, where an EAOB was employed to estimate total disturbances, including unmodeled dynamics and environmental disturbances. Instead of treating all disturbance sources as a unified variable in each DOF through the superposition principle, the focus here is on crafting an online system identification module capable of identifying uncertain hydrodynamic parameters using the estimated disturbances from the EAOB. The chapter encompasses a review of relevant AMPC literature featuring data-augmented models, the methodology behind the proposed identification algorithm and AMPC implementation, results of estimation accuracy and control performance, and conclusions. This chapter has been previously accepted as part of author's work in the [34].

4.1 Literature Review

The literature review in Section 3.1 already delves into other control methods commonly used for UUVs, including PID, SMC, DOBC, and other improved MPC methods. In this chapter's literature review, the focus shifts primarily towards control methods with

data-driven/data-augmented model.

Neural Network (NN)-based control approaches, classified as adaptive control methods, effectively manage parametric uncertainties by learning and adapting to evolving environments and system dynamics. Unlike conventional techniques, NN-based control leverages NNs to approximate system dynamics, adjusting network parameters based on data and feedback. This adaptability empowers control systems to navigate variations, uncertainties, and disturbances, bolstering robustness and flexibility. NN-based control excels in handling complex and nonlinear systems by capturing intricate patterns and relationships, ensuring precise control in highly uncertain scenarios. For instance, a hybrid coordination method utilizing reinforcement learning to online learn system behavior was implemented in an AUV [35]. A robust neural network approximation-based outputfeedback tracking controller has also been devised to effectively counter uncertainties [36]. Moreover, radial basis function neural networks have been integrated to compensate for unknown dynamics and disturbances in MPC, enhancing path following performance in surface ships [37]. Nonetheless, proving the system stability of NN-based control methods is often theoretically challenging, necessitating validation primarily through experimental evidence. Additionally, the efficacy of neural network adaptive controllers heavily relies on the number of neural network nodes, leading to a significant computational burden that hampers practical implementation in engineering applications.

Conversely, the fusion of Gaussian Process (GP)s with MPC has emerged as a potent strategy to tackle the aforementioned challenges [38]. GPs demand less training data and ensure system security. In 2021, GPs were applied to model unmanned quadrotor systems and integrated into the MPC framework [8]. Experimental results showcase GP's ability to discern the complex aerodynamic effects of quadrotors, achieving efficient and precise control. In [39], a sample-efficient probabilistic MPC was proposed to enhance control robustness against noise and disturbances, validated through a USV experiment. These endeavors underscore that GP, as a potent nonparametric plant in MPC, inherently

considers model uncertainties. Nonetheless, the applicability and convergence speed of these controllers are constrained by the interdependency of vehicle dynamic and kinematic models.

The methods aforementioned primarily belong to offline system identification, necessitating initial collection of training data. Various online system identification techniques have also been explored. Online system identification permits systems to adapt promptly to environment or system dynamics changes, offering more current parameter estimates. This adaptability enables swift responses to operational variations or disturbances, making it apt for applications requiring rapid adjustments. Online system identification can potentially be more cost-effective in scenarios mandating continuous monitoring and adaptation, obviating the need for recurrent large dataset collection for parameter estimation. In [40], a state variable filter and recursive least square estimator were developed to estimate unknown hydrodynamic parameters for an AUV, showcasing superior prediction accuracy, computational efficiency, and training time compared to conventional offline identification methods. An online system identification problem was also proposed in [41], estimating unknown parameters in nonlinear system dynamics without persistent excitation based on state-derivative estimation, demonstrating convergence to steady-state parameter estimates. Furthermore, an incremental support vector regression method was introduced to sequentially learn the UUV's model from data streams, highlighting its adaptability to dynamic changes in the robot's behavior [42].

However, these methods typically regard dynamics as static constructs. Hence, any alterations in the mechanical structure of an UUV or the physical parameters of its surrounding fluid could significantly impact the integrity of its mathematical model without adaptive measures. Inspired by the aforementioned studies, an online system identification algorithm grounded in Recursive Least Square (RLS) is proposed, further incorporating Variable Forgetting Factor (VFF) to adapt to shifts in the UUV's dynamics.

4.2 Methodology

In the system identification section of this project, the impact of Coriolis and centripetal forces resulting from the added mass C_A is deemed insignificant. This is because in numerous real-world scenarios like underwater examinations or low-speed data gathering operations, the velocities of open-frame UUVs typically do not exceed a few meters per second. Therefore, the dynamics model can be expanded in each DOF as:

$$X = (m - X_{\dot{u}})\dot{u} - mrv + mqw + (-X_u - X_{u|u|}|u|)u + (W - B)\sin\theta - X_{\text{env}},$$
(4.1)

$$Y = (m - Y_{\dot{v}})\dot{v} + mru - mpw + (-Y_v - y_{v|v|}|v|)v$$

$$- (W - B)\cos\theta\sin\phi - Y_{\text{env}},$$

$$(4.2)$$

$$Z = (m - Z_{\dot{w}})\dot{w} - mqu + mpv + (-Z_w - Z_{w|w|}|w|)w - (W - B)\cos\theta\cos\phi - Z_{\text{env}},$$
(4.3)

$$K = (I_x - K_{\dot{p}})\dot{p} + (I_z - I_y)qr + (-K_p - K_{p|p|}|p|)p + z_q W \cos\theta \sin\phi - K_{\text{env}},$$
(4.4)

$$M = (I_y - M_{\dot{q}})\dot{q} + (I_x - I_z)pr + (-M_q - M_{q|q|}|q|)q + z_q W \sin\theta - M_{\text{env}},$$
(4.5)

$$N = (I_z - N_{\dot{r}})\dot{r} + (I_y - I_x)pq + (-N_r - N_{r|r|}|r|)r - N_{\text{env}}.$$
(4.6)

While it is possible to calculate the hydrodynamic added mass coefficients of torpedoshaped UUVs by assuming the vehicle as an ellipsoid, such as the study in [43], it is challenging to directly calculate the added mass coefficients of open-frame UUVs like BlueROV2. Thus, in this work the added mass M_A is estimated by the online system identification. In the meantime, the hydrodynamic damping coefficients are commonly identified through experiment data, which are difficult to be calculated directly. Thus, damping forces $\mathbf{D}(\mathbf{v})$ with both linear and nonlinear damping coefficients are also treated as variable parameters to be estimated.

4.2.1 Problem Formulation

The observer's disturbance estimation $\hat{\boldsymbol{w}}$ includes the superposition of the environmental disturbance $\boldsymbol{\tau}_{\text{env}}$ and the unmodeled dynamics $\Delta \boldsymbol{\tau}$. Meanwhile, the unmodeled dynamics encompass the added mass \boldsymbol{M}_A (Equation 2.17) and linear and nonlinear damping coefficients (Equation 2.22) as detailed in Section 2.2. Hence, $\hat{\boldsymbol{w}}$ can be expressed as:

$$\hat{\boldsymbol{w}} = \boldsymbol{\tau}_{\text{env}} + \Delta \boldsymbol{\tau}
= \boldsymbol{M}_{A} \dot{\boldsymbol{v}} + \boldsymbol{D}_{L} \boldsymbol{v} + \boldsymbol{D}_{\text{NL}} |\boldsymbol{v}| \boldsymbol{v} + \boldsymbol{\tau}_{\text{env}}.$$
(4.7)

In this section, the surge dynamics in Equation 4.1 is discussed as an example, while the rest dynamics in Equation 4.2, 4.3, and 4.6 can also be implemented in a similar manner. Therefore, Equation 4.7 can be reconstructed for the surge dynamics as:

$$\hat{X}_{w} = \begin{bmatrix} \dot{u} & u & |u|u & 1 \end{bmatrix} \begin{bmatrix} X_{\dot{u}} \\ X_{u} \\ X_{u|u|} \\ X_{\text{ext}} \end{bmatrix}$$

$$(4.8)$$

where four unknown parameters can be denoted as

$$\Theta = \begin{bmatrix} X_{\dot{u}} & X_u & X_{u|u|} & X_{\text{ext}} \end{bmatrix}^{\top}.$$
 (4.9)

The identification problem involves determining the values of parameters using input/output discrete data while meeting specific goodness-of-fit constraints between predicted data and measurements. Therefore, the Θ can be identified by solving the cost function:

$$\underset{\boldsymbol{\Theta}^{\top} = [X_{\dot{u}}, X_u, X_{\text{ext}}]}{\operatorname{arg \, min}} J(\boldsymbol{\Theta}) = \sqrt{\frac{1}{N} \sum_{k=1}^{k=N} \left[y_k - \boldsymbol{\Theta}^{\top} \boldsymbol{\Phi}_k \right]^2}$$
subject to $X_{\dot{u}}, X_u, X_{u|u|}, X_{\text{ext}} \in \Re$ (4.10)

where N is the total number of samples available, y_k is the observed output (which is equal to $\hat{X_w}$ in surge dynamics), and

$$\mathbf{\Phi}_k = \left[\begin{array}{ccc} \dot{u}_k & u_k & |u|u_k & 1 \end{array} \right]^\top. \tag{4.11}$$

4.2.2 Identification Algorithm

To find the optimal parameters for a cost function, a common approach is to use the Least Square (LS) method. LS identifies parameters by minimizing the sum of the squared errors between predicted and observed values. In contrast to LS, which performs regression based on offline collected data, the RLS algorithm operates online. RLS processes data sequentially and updates parameter estimates as new data becomes available. The distinguishing feature of RLS-VFF is the incorporation of a forgetting factor, which enables a trade-off between tracking time-varying parameters and robustness to noise. The forgetting factor determines the weight assigned to past data points relative to recent data points when updating parameter estimates. A forgetting factor close to 1 places more emphasis on past rewards, resulting in low misadjustment but reduced adaptation ability. Conversely, a forgetting factor closer to 0 indicates that the agent prioritizes recent rewards, leading to high adaptation ability but potential susceptibility to outlier data and instability.

In the standard RLS-FF algorithm, the forgetting factor is typically set as a constant value. However, in this research, the forgetting factor is considered as a variable that can be dynamically adjusted based on the outcome of the F-test. The F-test is a statistical test used to compare the variances of two samples. In this context, it is employed to compare the prediction error variance of two windows of past RLS estimation results: a long window and a short window. The purpose of this comparison is to determine whether the variance has increased. The F-test statistic, denoted as F_k , is calculated as follows:

$$F_k = \frac{\sigma_n^2}{\sigma_d^2} = \frac{\frac{1}{n} \sum_{i=k-n}^n (e_i - \mu_n)^2}{\frac{1}{d} \sum_{i=k-d}^d (e_i - \mu_d)^2}$$
(4.12)

where n represents the number of samples in the short window, d represents the number of samples in the long window, σ_n^2 is the prediction error variance with n samples, σ_d^2 is the prediction error variance with d samples, and $d > n \ge 1$. The prediction error e_k can be computed as the difference between the observed output y_k and the parameter estimate at time k-1:

$$e_k = y_k - \hat{\boldsymbol{\Theta}}_{k|k-1}^T \boldsymbol{\Phi}_k. \tag{4.13}$$

By comparing the variance of the prediction errors in the short and long windows, the F-test provides insights into whether the system dynamics have changed significantly. If the F-test statistic exceeds a predefined threshold γ , it indicates that the variance has increased, suggesting a change in the system dynamics. In such cases, the forgetting factor is adjusted to respond to these changes and maintain accurate estimation:

$$\lambda_k = \begin{cases} \lambda_{k-1} + \Delta \lambda & \text{if } F_k < \gamma \\ \lambda_{k-1} - \Delta \lambda & \text{otherwise} \end{cases}$$
 (4.14)

where $\Delta \lambda$ represents the adjustment value for the forgetting factor.

This approach of using the F-test to adapt the forgetting factor in RLS-VFF enhances the algorithm's ability to track time-varying system dynamics, resulting in improved estimation performance.

In the initialization stage of the RLS-VFF algorithm, the parameter estimation $\hat{\Theta}$ is initialized to zero. Meanwhile, the initial value of the error covariance matrix P is determined based on the forgetting factor λ :

$$\hat{\boldsymbol{\Theta}}_{k=0} = 0$$

$$\boldsymbol{P}_{k=0} = \frac{1}{\lambda} \boldsymbol{I}$$
(4.15)

where I is the identity matrix.

The RLS-VFF algorithm operates similarly to the Kalman filters family. At time k, it calculates the Kalman gain K_k using the forgetting factor λ , the error covariance matrix \mathbf{P} from time k-1, and the regression factor $\mathbf{\Phi}_k$. Subsequently, the parameter estimation $\hat{\mathbf{\Theta}}_{k|k}$ is updated based on the Kalman gain and the error, and the error covariance matrix $\mathbf{P}_{k|k}$ is also updated accordingly. The recursive process can be formulated as:

$$K_{k} = \frac{\boldsymbol{P}_{k|k-1}\boldsymbol{\Phi}_{k}}{\lambda + \boldsymbol{\Phi}_{k}^{T}\boldsymbol{P}_{k|k-1}\boldsymbol{\Phi}_{k}}$$

$$\hat{\boldsymbol{\Theta}}_{k|k} = \hat{\boldsymbol{\Theta}}_{k|k-1} + K_{k}\boldsymbol{e}_{k}$$

$$\boldsymbol{P}_{k|k} = \frac{1}{\lambda} \left(\boldsymbol{P}_{k|k-1} - K_{k}\boldsymbol{\Phi}_{k}^{T}\boldsymbol{P}_{k|k-1} \right).$$

$$(4.16)$$

4.2.3 MPC Implementation

Here the MPC optimization problem in Equation 3.22 is reformulated as:

$$\min_{\boldsymbol{u}} J = \sum_{k=T_0}^{T_{N-1}} \left[\|\boldsymbol{e}_k\|_{\boldsymbol{Q}_c}^2 + \|\boldsymbol{u}_k\|_{\boldsymbol{R}_c}^2 \right] + \|\boldsymbol{e}_{T_N}\|_{\boldsymbol{Q}_N}$$
s.t. $\boldsymbol{e}_k = h\left(\boldsymbol{x}_k, \boldsymbol{u}_k\right) - \boldsymbol{y}_{ref,k}$

$$\boldsymbol{u}_k \in \mathbb{U}, \quad \boldsymbol{x}_k \in \mathbb{X}, \quad \boldsymbol{x}_{T_N} \in \mathbb{X}_N$$
(4.17)

where T_0 represents the initial time step, and T_N denotes the final time step within a prediction horizon. The matrices Q_c , R_c , and Q_N denote the weighting matrices used in optimization process. Based on multiple shooting method, the optimization problem at time t = k becomes:

$$\min_{\boldsymbol{x},\boldsymbol{u}} J_k = \sum_{i=k}^{k+N-1} l\left(\boldsymbol{x}_i, \boldsymbol{u}_i\right) + l_f\left(\boldsymbol{x}_{k+N}, \boldsymbol{u}_{k+N}\right)$$
s.t. $\boldsymbol{u}_i \in \mathbb{U}, \quad \boldsymbol{x}_i \in \mathbb{X}, \quad \boldsymbol{x}_{t_N} \in \mathbb{X}_N$

$$(4.18)$$

where $l(\cdot)$ denotes the positive definite function that related to the stage cost, and $l_f(\cdot)$ is the positive definite function that related to the terminal cost.

The comprehensive adaptive MPC framework is outlined in Algorithm 1.

Algorithm 1 Adaptive MPC with online system identification

```
1: Initialization:
           Initialize EAOB, RLS-VFF based on Equation 3.13, 4.15
 2:
 3: while t>0 do
 4:
                 Measure \boldsymbol{z} = [\boldsymbol{\eta}; \boldsymbol{v}; \boldsymbol{\tau}]
                 Estimate \hat{\boldsymbol{x}} = [\hat{\boldsymbol{\eta}}; \hat{\boldsymbol{v}}; \hat{\boldsymbol{w}}] with EAOB by Equation 3.14, 3.15
 5:
                 Calculate F_k by Equation 4.12
 6:
           if F_k > \gamma then
 7:
                      Update forgetting factor \lambda_k = \lambda_{k-1} - \Delta \lambda
 8:
           else
 9:
                       Update forgetting factor \lambda_k = \lambda_{k-1} + \Delta \lambda
10:
                 Estimate \hat{\Theta} = [X_u X_u X_{u|u|} X_{\text{ext}}]^T with RLS-VFF by Equation 4.16
11:
                 Update MPC control law: \boldsymbol{\tau} = \boldsymbol{K}(\boldsymbol{A}\boldsymbol{u}) = \boldsymbol{M_{RB}}\dot{\boldsymbol{v}} + \boldsymbol{C}(\boldsymbol{v})\boldsymbol{v} + \boldsymbol{g}(\boldsymbol{\eta}) - \hat{\boldsymbol{\Theta}}^T\boldsymbol{\Phi}
12:
                 Solve the OCP to obtain the optimized control sequence u^*(s) by Equation
13:
     4.17
                 Implement the first element u_0^* in the optimized control sequence to the UUV
14:
15: end while
```

Figure 4.1 illustrates the control framework of the AMPC with online system identification proposed in this work, with the pink box highlights the adaptive mechanism involved in steps 5-11 in Algorithm 1.

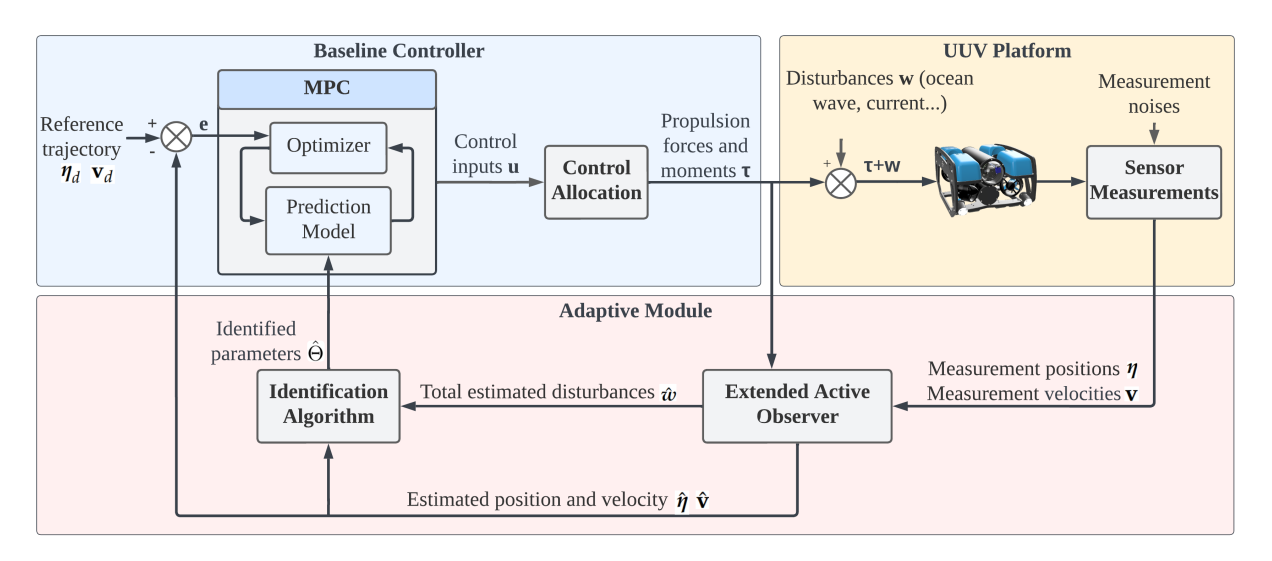


Figure 4.1: Block diagram of the proposed adaptive MPC scheme for the UUV, where the blue box illustrates baseline MPC and control allocation, the yellow box shows the UUV platform, and the pink module indicates the adaptive module with an observer and identification algorithm.

4.2.4 Stability Analysis

The stability analysis of the proposed AMPC has been obtained as a part of Author's work in the [44].

The assurance of MPC stability relies on the terminal cost and constraints. Hence, the subsequent assumption is made:

Assumption 3 For all $\mathbf{x} \in \mathbb{X}_N$, the terminal cost $l_f(\cdot)$ is a continuous Lyapunov function such that:

$$l_f(h(\boldsymbol{x}, \boldsymbol{u})) - l_f(\boldsymbol{x}, \boldsymbol{u}) \le -l(\boldsymbol{x}, \boldsymbol{u}). \tag{4.19}$$

Therefore, the lemma can be published as:

Lemma 1 With the optimization problem defined in Equation 4.17, the MPC controller is asymptotically stable if the following conditions hold:

- 1) $\mathbb{U}, \mathbb{X}, \mathbb{X}_N \neq \emptyset$.
- 2) Only the $\mathbf{u}(k)$ is inputted to the optimization process.

3) N is sufficiently large and global optimal can be acquired at each time k.

4)
$$J_k = 0 \text{ if } \boldsymbol{x}, \boldsymbol{u} = 0$$

- 5) The prediction model is unbiased and has no measurement noises
- 6) Assumption 3 holds

Proof 1 Define Lyapunov function as $V_k = \min J_k$, thus:

$$V_{k} = \sum_{i=k}^{k+N-1} l(\mathbf{x}_{i}, \mathbf{u}_{i}) + l_{f}(\mathbf{x}_{k+N}, \mathbf{u}_{k+N}).$$
(4.20)

Therefore, V_k is positive definite. Similarly,

$$V_{k+1} = \sum_{i=k+1}^{k+N} l\left(\boldsymbol{x}_{i}, \boldsymbol{u}_{i}\right) + l_{f}\left(\boldsymbol{x}_{k+1+N}, \boldsymbol{u}_{k+1+N}\right)$$

$$= \sum_{i=k}^{k+N-1} l\left(\boldsymbol{x}_{i}, \boldsymbol{u}_{i}\right) + l_{f}\left(\boldsymbol{x}_{k+N}, \boldsymbol{u}_{k+N}\right)$$

$$+ l_{f}\left(\boldsymbol{x}_{k+1+N}, \boldsymbol{u}_{k+1+N}\right) - l\left(\boldsymbol{x}_{k}, \boldsymbol{u}_{k}\right)$$

$$- l_{f}\left(\boldsymbol{x}_{k+N}, \boldsymbol{u}_{k+N}\right) + l\left(\boldsymbol{x}_{k+N}, \boldsymbol{u}_{k+N}\right).$$

$$(4.21)$$

Using Condition 4 in Lemma 1 and Equation 4.20 yields:

$$V_{k+1} = V_k - l\left(\boldsymbol{x}_k, \boldsymbol{u}_k\right) + l_f\left(\boldsymbol{x}_{k+1+N}, \boldsymbol{u}_{k+1+N}\right)$$

$$- l_f\left(\boldsymbol{x}_{k+N}, \boldsymbol{u}_{k+N}\right) + l\left(\boldsymbol{x}_{k+N}, \boldsymbol{u}_{k+N}\right).$$

$$(4.22)$$

Using the facts that $-l(\boldsymbol{x}_{k+1}, \boldsymbol{u}_k) \leq 0$ and $l_f(\boldsymbol{x}_{k+1+N}, \boldsymbol{u}_{k+1+N}) - l_f(\boldsymbol{x}_{k+N}, \boldsymbol{u}_{k+N}) + l(\boldsymbol{x}_{k+N}, \boldsymbol{u}_{k+N}) \leq 0$, the difference equation of V_k is therefore semi-negative definite. The proof is hence concluded.

4.3 Results

To perform online system identification, the UUV's motion in each DOF must be captured for training and regression with the RLS-VFF. Therefore, a reference trajectory is specified for training purposes and provided to the MPC before executing other trajectory tracking tasks. The entire training process spans 40 seconds, with the following breakdown: 1) Surge dynamics training: begins at 0 seconds and concludes at 10 seconds; 2) Sway dynamics training: commences at 10 seconds and finishes at 20 seconds; 3) Heave dynamics training: initiates at 20 seconds and terminates at 30 seconds; 4) Yaw dynamics training: starts at 30 seconds and concludes at 40 seconds.

In this study, the number of samples in the short and long windows are set as n=10 and d=50. A smaller n makes the F-test more sensitive to system changes, resulting in a fast adjusting forgetting factor. Additionally, the threshold value γ is set to 0.8. The estimated parameters in $\hat{\Theta}$ obtained using the RLS-VFF algorithm are compared with those obtained using the standard RLS-FF algorithm with a forgetting factor of 0.98. Since the work is conducted in Gazebo, the parameters defined in the Gazebo's URDF file are used as a benchmark for comparison with the estimation results.

Figure 4.2 presents the system identification results in the absence of additional environmental disturbances. In this scenario, the system can be considered as slowly changing. Consequently, the F-test value remains below the threshold γ for most of the time, causing the variable forgetting factor to approach 1. As a result, the estimation results obtained using the RLS-VFF, represented by the blue line, exhibit a slower convergence rate but higher stability, resulting in a smoother line. The estimation results exhibit greater fluctuations in the Z-axis may caused by the influence of gravity and buoyancy.

On the other hand, Figure 4.3 demonstrates the system identification results with the introduction of additional environmental disturbances of 5N in the x_i , y_i , and z_i directions in the IRF. Since the environmental disturbances term τ_{env} is defined in the BRF in the

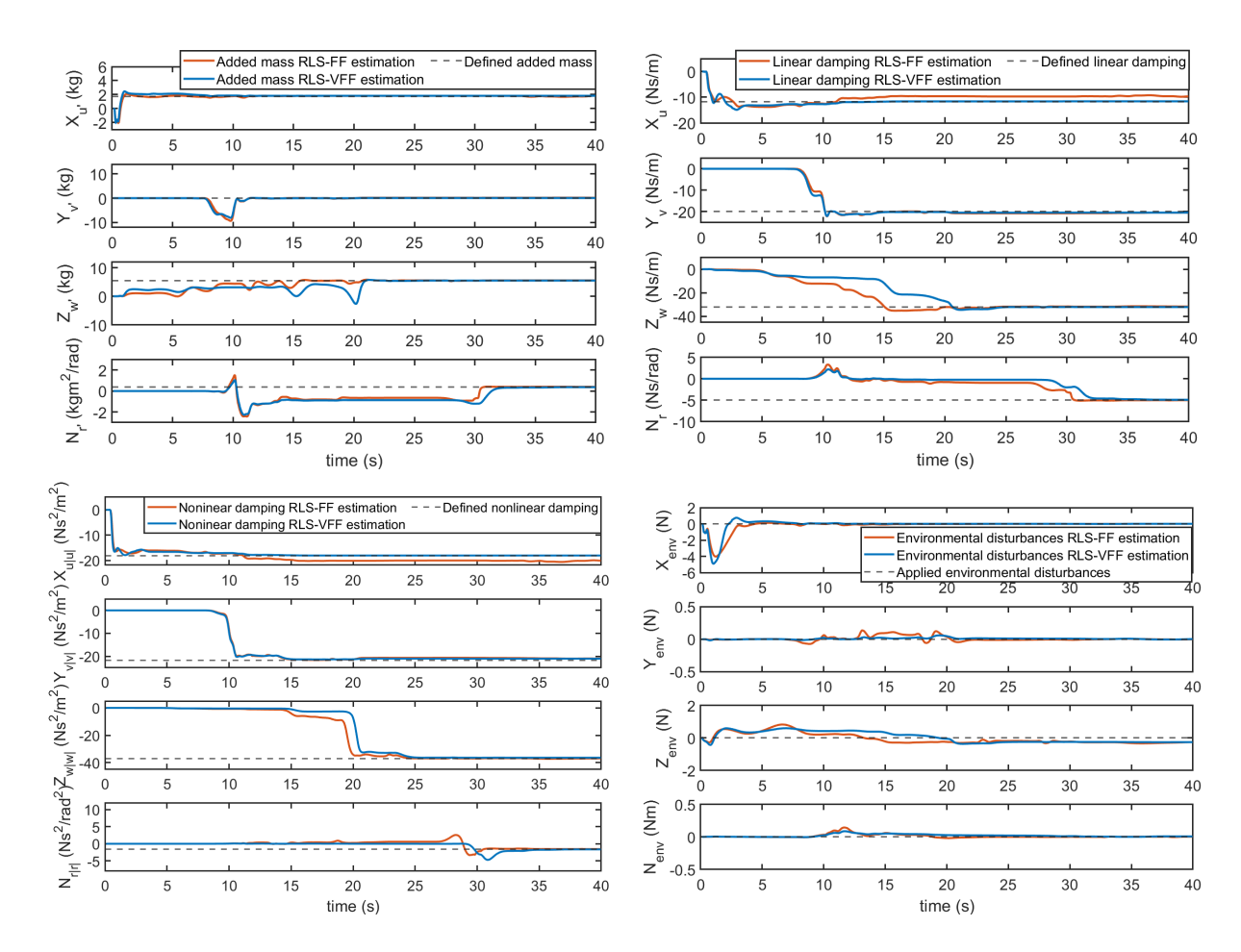


Figure 4.2: Online system identification results of added mass, linear damping coefficients, nonlinear damping coefficients, and environmental disturbances using the RLS-FF and the RLS-VFF during the training process without applied environmental disturbances.

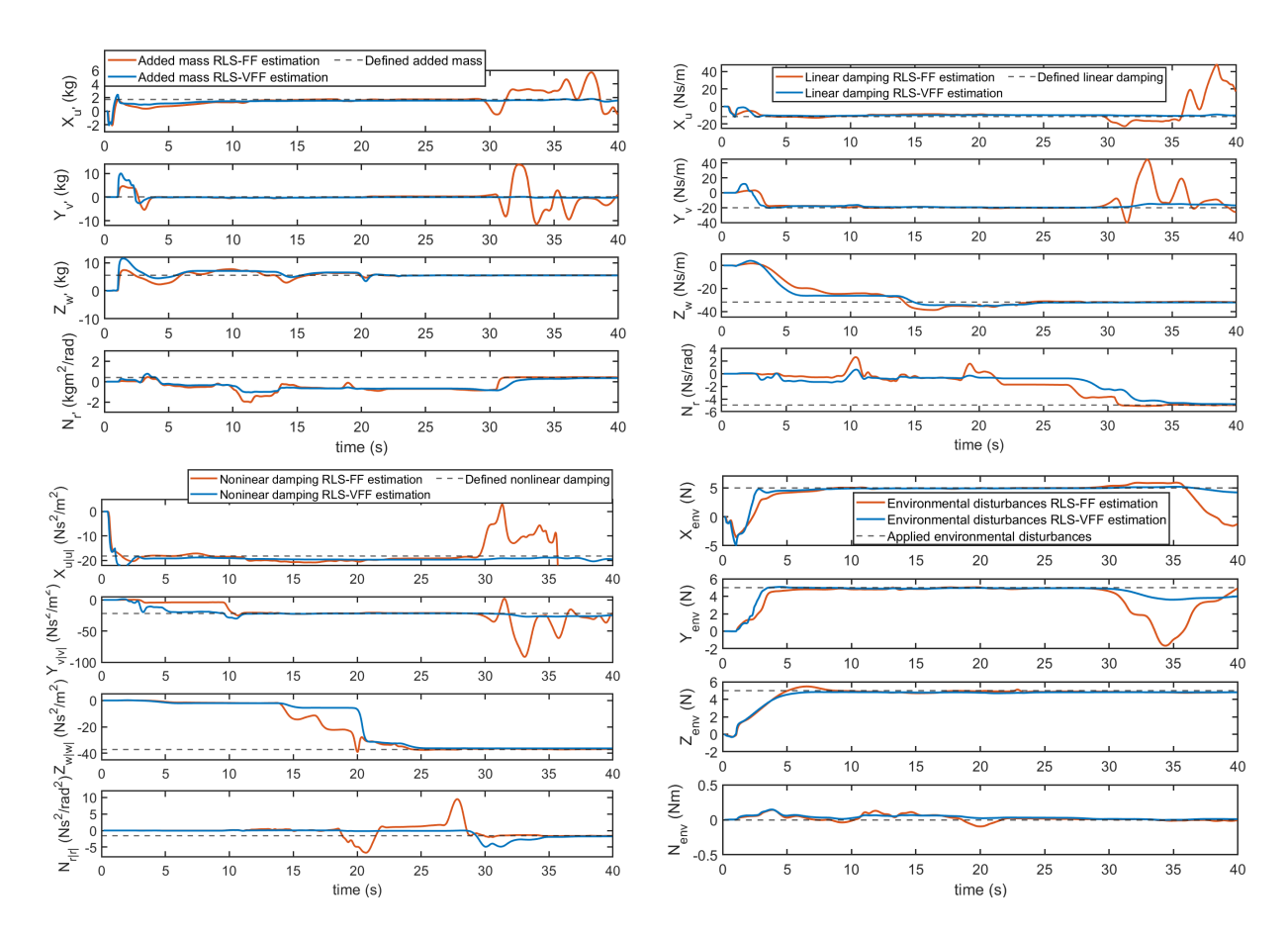


Figure 4.3: Online system identification results of added mass, linear damping coefficients, nonlinear damping coefficients, and environmental disturbances using the RLS-FF and the RLS-VFF during the training process with applied environmental disturbances.

UUV dynamics model, it has been transformed to the IRF using a rotation matrix for a clearer presentation of the results. After 30 seconds, the orientation of the UUV begins to change to train the yaw dynamics. Consequently, the environmental disturbances acting on the BRF also start to change, leading to a faster changing system. In this situation, the standard RLS-FF struggles to adapt to these changes quickly and stably, resulting in significant chattering in the red line. In contrast, the proposed RLS-VFF still manages to converge to the defined parameters swiftly.

The performance of the proposed AMPC algorithm is evaluated in comparison to a standard MPC controller and a PID controller. Both the AMPC and the standard MPC employ the same control parameters, as detailed in Table 3.3. Meanwhile, the PID con-

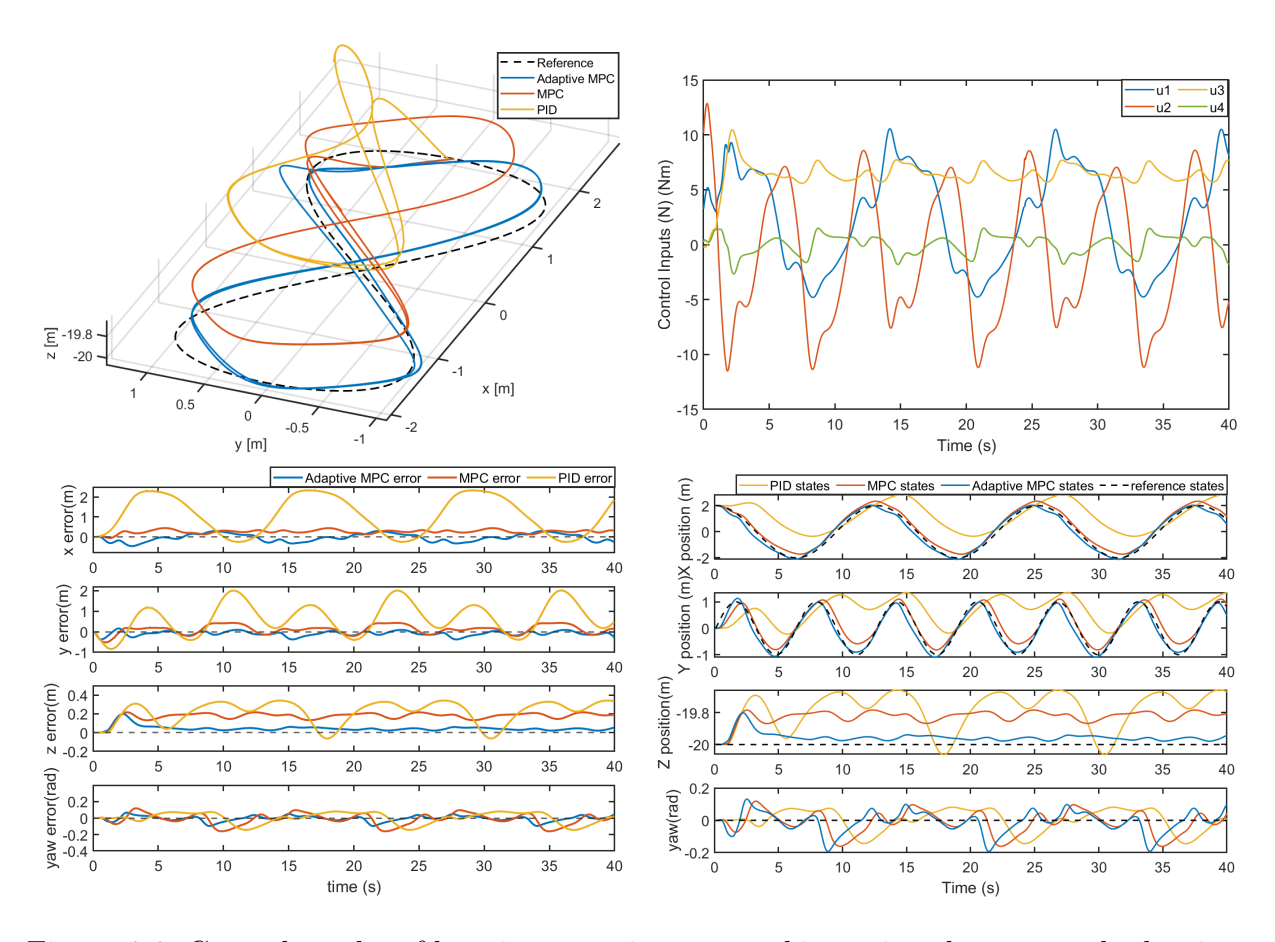


Figure 4.4: Control results of lemniscate trajectory tracking using the proposed adaptive MPC, standard MPC, and PID controllers.

troller's control gains are specified in Table 3.4. A lemniscate trajectory with amplitude of 2 meters is employed as trajectory tracking control problem for these controllers. Furthermore, the additional environmental disturbances of 10N are also applied in the x_i , y_i , and z_i directions in the IRF.

Figure 4.4 presents the control outcomes achieved by the AMPC, standard MPC, and PID controllers in tracking the lemniscate trajectory. The subplots indicate the three-dimensional trajectory tracking results, control inputs, tracking errors, and tracking states, respectively. These results demonstrate the substantial improvement in control performance achieved by employing the proposed adaptive MPC algorithm, even when faced with a highly nonlinear tracking problem and the presence of environmental disturbances.

4.4 Conclusion

In this study, an effective adaptive control method is proposed by integrating a fast system identification module with MPC for UUVs' motion control in complex underwater environments. Unlike conventional offline system identification, the proposed approach utilizes RLS-VFF for online real-time adaptation of the system model when new measurement data is available. This incremental update of model parameters enables continuous learning and tracking of system dynamics. Additionally, RLS-VFF offers computational efficiency by avoiding the need to recompute the regression from scratch for each new data point. By incorporating a variable forgetting factor, the algorithm determines the weight between recent and past data based on the F-test. The F-test assesses if the system has undergone significant changes, and if so, the algorithm gradually reduces the influence of older data to enable rapid and stable adaptation. By improving the accuracy of the prediction model in MPC and compensating for environmental disturbances, the proposed method achieves a reliable controller with the capability of adapting to unknown environments and delivering superior control performance.

Chapter 5

Conclusions and Future Work

This thesis explores the application of two improved MPC strategies to enable an UUV to navigate autonomously within intricate marine settings surrounding underwater structures. These controllers are engineered to adapt to unforeseen environmental perturbations and changing system dynamics.

Chapter 2 delves into the UUV platform utilized, equipped with a variety of sensors that lay the groundwork for future autonomous navigation. Additionally, the UUV dynamic model is established based on the Fossen model [11].

In Chapter 3, the initial proposed improved MPC is introduced. Initially, a DOBMPC is developed to integrate unmodeled dynamics into the disturbance model, alongside environmental disturbances, within the MPC's predictive framework. Various external disturbances are simulated for evaluation, such as constant currents, periodic waves, and their superposition. Diverse control tasks, including dynamic positioning, circular trajectory tracking, and lemniscate tracking, are employed for assessment. Results indicate that compared to PID and baseline MPC approaches, the proposed DOBMPC exhibits the lowest RMSE in tracking. While the simulation demonstrates the DOBMPC's efficacy in mitigating disturbances, it's noted that excessively large and rapidly changing unidentified hydrodynamic damping forces, if directly integrated as part of the total disturbance,

may impede the MPC optimizer's performance.

Subsequently, an AMPC incorporating an online system identification algorithm, based on the DOBMPC, is presented in Chapter 4. This algorithm utilizes estimated total disturbances from the Extended Augmented Observer-based approach as input to iteratively estimate hydrodynamic coefficients, encompassing hydrodynamic added mass, linear damping coefficients, and nonlinear damping coefficients. To ensure identification accuracy, the algorithm employs an F-test to compare prediction error variances and adjust the forgetting factor as necessary. Comparative analysis demonstrates that, in contrast to the baseline RLS-FF method, the proposed identification algorithm converges more swiftly and robustly towards the true values, thereby enhancing the control performance of the AMPC.

The future direction of this research focuses on developing a deep learning-based Tube Model Predictive Control (TMPC) framework to enhance the robustness and performance of UUVs in uncertain underwater environments. Learning-based control involves constructing data-driven models of the system dynamics for planning and trajectory optimization; however, accurate uncertainty quantification remains a critical challenge due to the presence of external disturbances, model inaccuracies, and the inherent complexity of the system. Traditional uncertainty propagation methods often rely on restrictive assumptions, which can limit controller performance. To overcome this, we propose using deep learning techniques to directly learn uncertainty from data through quantile regression, enabling a flexible representation of trajectory distributions. This approach forms a tube around the nominal trajectory that captures the variability of future system behavior. The resulting tube will be integrated into the MPC framework, forming a TMPC that ensures constraint satisfaction with high probability and improves closed-loop performance. The implementation will begin with data collection from simulations under various disturbances, followed by training a neural network to model both the dynamics and associated uncertainty. The learned quantile tubes will then be embedded into the optimization problem of MPC, reformulating constraints to account for predicted uncertainty bounds. This approach will be validated through extensive simulations using platforms like Gazebo and the UUV Simulator, comparing it with baseline controllers, and eventually optimized for real-time deployment in real-world scenarios. By integrating uncertainty quantification into the control framework, the proposed TMPC method aims to provide a robust and effective solution for reliable operation of autonomous marine systems.

Bibliography

- [1] J. Mao, G. Song, S. Hao, M. Zhang, and A. Song, "Development of a lightweight underwater manipulator for delicate structural repair operations," *IEEE Robotics and Automation Letters*, vol. 8, no. 10, pp. 6563–6570, 2023.
- [2] C. Mai, M. v. Benzon, F. F. Sørensen, S. S. Klemmensen, S. Pedersen, and J. Liniger, "Design of an autonomous rov for marine growth inspection and cleaning," in 2022 IEEE/OES Autonomous Underwater Vehicles Symposium (AUV), 2022, pp. 1–6.
- [3] S. Hou, D. Jiao, B. Dong, H. Wang, and G. Wu, "Underwater inspection of bridge substructures using sonar and deep convolutional network," *Advanced Engineering Informatics*, vol. 52, p. 101545, 2022.
- [4] M. W. Hasan and N. H. Abbas, "Disturbance rejection for underwater robotic vehicle based on adaptive fuzzy with nonlinear pid controller," ISA transactions, vol. 130, pp. 360–376, 2022.
- [5] Z. Yan, M. Wang, and J. Xu, "Robust adaptive sliding mode control of underactuated autonomous underwater vehicles with uncertain dynamics," *Ocean Engineering*, vol. 173, pp. 802–809, 2019.
- [6] H. Wei and Y. Shi, "Mpc-based motion planning and control enables smarter and safer autonomous marine vehicles: perspectives and a tutorial survey," *IEEE/CAA Journal of Automatica Sinica*, vol. 10, no. 1, pp. 8–24, 2023.

- [7] J. Arcos-Legarda and Á. Gutiérrez, "Robust model predictive control based on active disturbance rejection control for a robotic autonomous underwater vehicle," *Journal* of Marine Science and Engineering, vol. 11, no. 5, p. 929, 2023.
- [8] G. Torrente, E. Kaufmann, P. Föhn, and D. Scaramuzza, "Data-driven mpc for quadrotors," *IEEE Robotics and Automation Letters*, vol. 6, no. 2, pp. 3769–3776, 2021.
- [9] Y. Hu, B. Li, B. Jiang, J. Han, and C.-Y. Wen, "Disturbance observer-based model predictive control for an unmanned underwater vehicle," *Journal of Marine Science* and Engineering, vol. 12, no. 1, 2024.
- [10] B. Robotics, "Bluerov2: The world's most affordable high-performance rov," BlueROV2 Datasheet; Blue Robotics: Torrance, CA, USA, 2016.
- [11] T. I. Fossen, Handbook of marine craft hydrodynamics and motion control. John Wiley & Sons, 2011.
- [12] T. G. Chondros, "Archimedes (287–212 bc)," in Distinguished Figures in Mechanism and Machine Science: Their Contributions and Legacies Part 1. Springer, 2007, pp. 1–30.
- [13] C. Woolsey, "Review of marine control systems: Guidance, navigation, and control of ships, rigs and underwater vehicles," *Journal of Guidance, Control, and Dynamics*, vol. 28, pp. 574–575, 05 2005.
- [14] L. Liu, L. Zhang, G. Pan, and S. Zhang, "Robust yaw control of autonomous underwater vehicle based on fractional-order pid controller," *Ocean Engineering*, vol. 257, p. 111493, 2022.
- [15] Z. Bingul and K. Gul, "Intelligent-pid with pd feedforward trajectory tracking control of an autonomous underwater vehicle," *Machines*, vol. 11, no. 2, p. 300, 2023.

- [16] A. Healey and D. Lienard, "Multivariable sliding mode control for autonomous diving and steering of unmanned underwater vehicles," *IEEE Journal of Oceanic Engineer*ing, vol. 18, no. 3, pp. 327–339, 1993.
- [17] T. Lv, J. Zhou, Y. Wang, W. Gong, and M. Zhang, "Sliding mode based fault tolerant control for autonomous underwater vehicle," *Ocean Engineering*, vol. 216, p. 107855, 2020.
- [18] M. Kamel, T. Stastny, K. Alexis, and R. Siegwart, "Model predictive control for trajectory tracking of unmanned aerial vehicles using robot operating system," Robot Operating System (ROS) The Complete Reference (Volume 2), pp. 3–39, 2017.
- [19] A. Veksler, T. A. Johansen, F. Borrelli, and B. Realfsen, "Dynamic positioning with model predictive control," *IEEE Transactions on Control Systems Technology*, vol. 24, no. 4, pp. 1340–1353, 2016.
- [20] L. Medagoda and S. B. Williams, "Model predictive control of an autonomous underwater vehicle in an in situ estimated water current profile," in 2012 Oceans Yeosu, 2012, pp. 1–8.
- [21] C. Shen, Y. Shi, and B. Buckham, "Trajectory tracking control of an autonomous underwater vehicle using lyapunov-based model predictive control," *IEEE Transactions on Industrial Electronics*, vol. 65, no. 7, pp. 5796–5805, 2018.
- [22] Y. Cao, B. Li, Q. Li, A. A. Stokes, D. M. Ingram, and A. Kiprakis, "A nonlinear model predictive controller for remotely operated underwater vehicles with disturbance rejection," *IEEE Access*, vol. 8, pp. 158622–158634, 2020.
- [23] B. M. Patre, P. S. Londhe, L. M. Waghmare, and S. Mohan, "Disturbance estimator based non-singular fast fuzzy terminal sliding mode control of an autonomous underwater vehicle," *Ocean Engineering*, vol. 159, pp. 372–387, 2018.

- [24] G. V. Lakhekar, L. M. Waghmare, and R. G. Roy, "Disturbance observer-based fuzzy adapted s-surface controller for spatial trajectory tracking of autonomous underwater vehicle," *IEEE Transactions on Intelligent Vehicles*, vol. 4, no. 4, pp. 622–636, 2019.
- [25] Y. Dai, D. Wu, S. Yu, and Y. Yan, "Robust control of underwater vehicle-manipulator system using grey wolf optimizer-based nonlinear disturbance observer and h-infinity controller," *Complexity*, vol. 2020, pp. 1–17, 2020.
- [26] R. I. Alfian, A. Ma'arif, and S. Sunardi, "Noise reduction in the accelerometer and gyroscope sensor with the kalman filter algorithm," *Journal of Robotics and Control* (*JRC*), vol. 2, no. 3, pp. 180–189, 2021.
- [27] Y. Bai, X. Wang, X. Jin, T. Su, J. Kong, and B. Zhang, "Adaptive filtering for mems gyroscope with dynamic noise model," *ISA transactions*, vol. 101, pp. 430–441, 2020.
- [28] J. Guerrero, J. Torres, V. Creuze, and A. Chemori, "Adaptive disturbance observer for trajectory tracking control of underwater vehicles," *Ocean Engineering*, vol. 200, p. 107080, 2020.
- [29] L. Chan, F. Naghdy, and D. Stirling, "Extended active observer for force estimation and disturbance rejection of robotic manipulators," Robotics and Autonomous Systems, vol. 61, no. 12, pp. 1277–1287, 2013.
- [30] R. E. Kalman and R. S. Bucy, "New results in linear filtering and prediction theory,"

 Journal of Fluids Engineering, vol. 84, 1961.
- [31] M. Diehl, H. G. Bock, H. Diedam, and P.-B. Wieber, "Fast direct multiple shooting algorithms for optimal robot control," Fast motions in biomechanics and robotics: optimization and feedback control, pp. 65–93, 2006.

- [32] R. Verschueren, G. Frison, D. Kouzoupis, N. van Duijkeren, A. Zanelli, R. Quirynen, and M. Diehl, "Towards a modular software package for embedded optimization," IFAC-PapersOnLine, vol. 51, no. 20, pp. 374–380, 2018.
- [33] M. M. M. Manhães, S. A. Scherer, M. Voss, L. R. Douat, and T. Rauschenbach, "UUV simulator: A gazebo-based package for underwater intervention and multirobot simulation," in OCEANS 2016 MTS/IEEE Monterey. IEEE, sep 2016.
- [34] Y. Hu, B. Li, and C.-Y. Wen, "Adaptive model predictive control with online system identification for an unmanned underwater vehicle," in 2024 Oceans - Singapore, 2024.
- [35] M. Carreras, J. Batlle, and P. Ridao, "Hybrid coordination of reinforcement learning-based behaviors for auv control," in *Proceedings 2001 IEEE/RSJ International Conference on Intelligent Robots and Systems. Expanding the Societal Role of Robotics in the Next Millennium (Cat. No.01CH37180)*, vol. 3, 2001, pp. 1410–1415 vol.3.
- [36] O. Elhaki and K. Shojaei, "A robust neural network approximation-based prescribed performance output-feedback controller for autonomous underwater vehicles with actuators saturation," *Engineering Applications of Artificial Intelligence*, vol. 88, p. 103382, 2020.
- [37] R. Li, J. Huang, X. Pan, Q. Hu, and Z. Huang, "Path following of underactuated surface ships based on model predictive control with neural network," *International Journal of Advanced Robotic Systems*, vol. 17, no. 4, p. 1729881420945956, 2020.
- [38] L. Hewing, K. P. Wabersich, M. Menner, and M. N. Zeilinger, "Learning-based model predictive control: Toward safe learning in control," *Annual Review of Control*, *Robotics, and Autonomous Systems*, vol. 3, no. 1, pp. 269–296, 2020.
- [39] Y. Cui, S. Osaki, and T. Matsubara, "Reinforcement learning boat autopilot: a sample-efficient and model predictive control based approach," in 2019 IEEE/RSJ

- International Conference on Intelligent Robots and Systems (IROS). IEEE, 2019, pp. 2868–2875.
- [40] Y. H. Eng, K. M. Teo, M. Chitre, and K. M. Ng, "Online system identification of an autonomous underwater vehicle via in-field experiments," *IEEE Journal of Oceanic Engineering*, vol. 41, no. 1, pp. 5–17, 2015.
- [41] E. Kayacan, S. Park, C. Ratti, and D. Rus, "Online system identification algorithm without persistent excitation for robotic systems: Application to reconfigurable autonomous vessels," in 2019 IEEE/RSJ International Conference on Intelligent Robots and Systems (IROS). IEEE, 2019, pp. 1840–1847.
- [42] B. Wehbe, M. Hildebrandt, and F. Kirchner, "A framework for on-line learning of underwater vehicles dynamic models," in 2019 International Conference on Robotics and Automation (ICRA). IEEE, 2019, pp. 7969–7975.
- [43] P. Cardenas and E. A. de Barros, "Estimation of auv hydrodynamic coefficients using analytical and system identification approaches," *IEEE Journal of Oceanic Engineering*, vol. 45, no. 4, pp. 1157–1176, 2019.
- [44] L.-Y. Lo, Y. Hu, B. Li, C.-Y. Wen, and Y. Yang, "An adaptive model predictive control for unmanned underwater vehicles subject to external disturbances and measurement noise," in 2024 15th Asian Control Conference (ASCC), 2024.